

## **ABSTRACT**

FOX, WILLIAM CARR. Investigating Nucleosynthesis in Massive AGB Stars with Transfer Reactions. (Under the direction of Richard Longland).

Abstract text ...

© Copyright 2023 by William Carr Fox

All Rights Reserved

Investigating Nucleosynthesis in Massive AGB Stars with Transfer Reactions

by  
William Carr Fox

A dissertation submitted to the Graduate Faculty of  
North Carolina State University  
in partial fulfillment of the  
requirements for the Degree of  
Doctor of Philosophy

Physics

Raleigh, North Carolina  
2023

APPROVED BY:

---

Christian Iliadis

---

Carla Frohlich

---

Matthew Green

---

John Classen

---

Richard Longland  
Chair of Advisory Committee

## **BIOGRAPHY**

The author was born in a small town ...

## TABLE OF CONTENTS

<b>List of Tables . . . . .</b>	<b>v</b>
<b>List of Figures . . . . .</b>	<b>vi</b>
<b>Chapter 1 Introduction . . . . .</b>	<b>1</b>
<b>Chapter 2 Nuclear Reactions in Stars . . . . .</b>	<b>2</b>
2.1 Introduction . . . . .	3
2.2 Reaction Rates . . . . .	3
2.2.1 Wide Resonances . . . . .	3
2.2.2 Narrow Resonances . . . . .	3
2.2.3 Gamow Window . . . . .	3
2.3 Abundance Evolution . . . . .	3
2.4 Transfer Reactions . . . . .	3
2.4.1 Optical Model . . . . .	3
2.4.2 Distorted Wave Born Approximation . . . . .	3
2.4.3 Spectroscopic Factors . . . . .	3
2.4.4 . . . . .	3
<b>Chapter 3 Rubidium Production in Massive AGB Stars . . . . .</b>	<b>4</b>
<b>Chapter 4 Experimental Nuclear Techniques . . . . .</b>	<b>5</b>
<b>Chapter 5 Data Acquisition System for the Focal-Plane Detector Package</b>	<b>6</b>
<b>Chapter 6 <math>^{39}\text{K}(p, \gamma)^{40}\text{Ca}</math> Constraints for Globular Cluster NGC 2419 . . . . .</b>	<b>7</b>
6.1 Introduction . . . . .	7
6.2 Globular Clusters . . . . .	7
6.3 NGC 2419 and the Mg–K Anticorrelation . . . . .	11
6.4 The Previous $^{39}\text{K}(p, \gamma)^{40}\text{Ca}$ Reaction Rate . . . . .	16
6.4.1 Longland <i>et al.</i> (2018) Evaluation . . . . .	16
6.4.2 Contributing Resonances . . . . .	18
6.4.3 Previous Proton-Transfer Measurements . . . . .	19
6.5 The $^{39}\text{K}(^3\text{He}, d)^{40}\text{Ca}$ Experiment . . . . .	20
6.5.1 Targets . . . . .	20
6.5.2 Focal-Plane Spectra . . . . .	21
6.5.3 Energy Shifts . . . . .	22
6.5.4 Silicon Detector Telescope . . . . .	22
6.5.5 Oxidized Spectra . . . . .	22
6.6 Bayesian Peak Fitting and Target Oxidation . . . . .	22
6.6.1 Bayesian Peak Fitting . . . . .	23
6.6.2 Fitting Peaks with Target Oxidation . . . . .	26
6.7 Cross Section Calculations and Si Detector Normalization . . . . .	29

6.7.1	Cross Sections . . . . .	29
6.7.2	Si Detector Normalization . . . . .	29
6.8	$^{39}\text{K}(^3\text{He}, d)^{40}\text{Ca}$ Analysis . . . . .	29
6.8.1	Energy Calibrations . . . . .	29
6.8.2	Cross Sections . . . . .	29
6.8.3	Oxidized Targets . . . . .	29
6.8.4	Spectroscopic Factors from DWBA Models . . . . .	29
6.8.5	Proton Partial Widths . . . . .	29
6.9	New $^{39}\text{K}(p, \gamma)^{40}\text{Ca}$ Reaction Rate . . . . .	29
6.10	Potassium Abundance in Reaction Network Calculations . . . . .	30
6.11	Conclusions . . . . .	30
	<b>Chapter 7 Summary and Conclusions . . . . .</b>	<b>42</b>
	<b>APPENDIX . . . . .</b>	<b>47</b>
	Appendix A $^{40}\text{Ca}$ Energy Calibrations . . . . .	48

## LIST OF TABLES

Table 6.1 Information on each run of the $^{39}\text{K}(^3\text{He}, d)^{40}\text{Ca}$ experiment, including the angle of the Enge, the target used, the magnetic field of the Enge, and the sort group (see text). . . . .	22
---	----

## LIST OF FIGURES

Figure 6.1	The O–Na anticorrelation of 1,200 red giants among all 19 globular clusters observed in the survey of Ref. [Car10]. Blue arrows indicate upper limits in O abundances, while lines separate different populations of red giants based on their relative O and Na richness. Primordial (P), extreme (E), and intermediate (I) populations are labeled in the first panel. See text for definitions of these populations. Adapted from [Car10].	9
Figure 6.2	The hydrogen burning mechanism driving the O–Na anticorrelation. Nuclei in blue are destroyed overall in the various cycles, while nuclei in red are produced. Shaded nuclei are stable. The first two stages of the CNO cycle (left), distinguished by the temperature-dependent branch at $^{15}\text{N}$ , lead to an overall depletion of oxygen. The $^{15}\text{N}(p, \gamma)^{16}\text{O}$ reaction is activated at about 40 MK. The Ne–Na cycle (right), occurring simultaneously at about the same activation temperature, leads to an overall production of sodium. The $^{23}\text{Na}(p, \gamma)^{24}\text{Mg}$ reaction activates at about 70 MK.	10
Figure 6.3	The observed Mg and K elemental abundances of red giants in NGC 2419 from Refs. [Muc12] (red) and [Coh12] (blue). Figure adapted from [Ili16].	12
Figure 6.4	The hydrogen burning mechanism driving the Mg–K anticorrelation in the globular cluster NGC 2419. The nucleosynthesis chain for the Mg depletion is the Mg–Al cycle, shown on the left-hand side. Whether the $^{26}\text{Al}^m$ isomer or the $^{26}\text{Al}^g$ ground state is populated, the result is $^{27}\text{Al}$ production, which repeats the cycle with $^{27}\text{Al}(p, \alpha)^{24}\text{Mg}$ . The main nucleosynthesis chain for the K enrichment is shown on the right-hand side with solid arrows. The $^{37}\text{Ar}(p, \gamma)^{38}\text{K}$ reaction proceeds at a much higher rate than $^{37}\text{Ar}(e^-, \nu)^{37}\text{Cl}$ electron capture at the stellar densities of interest. Nuclides in blue are destroyed and nuclides in red are produced in the overall nucleosynthesis. Shaded nuclides are stable.	13
Figure 6.5	Temperature-density conditions reproducing the Mg–K anticorrelation and other abundance patterns in NGC 2419, obtained by sampling $T$ , $\rho$ , $X_{\text{H}}$ , reaction rate probability densities, and initial abundances from a nuclear reaction network (see text). The $T$ – $\rho$ conditions for several polluter star candidates are represented by the black lines. Adapted from Ref. [Ili16].	14
Figure 6.6	Systematic effects of the $^{39}\text{K}(p, \gamma)^{40}\text{Ca}$ reaction rate influencing temperature-density conditions. The indicated variation factors ( $\alpha = 1/10, 1/5, 5, 10$ ) are applied to the reaction rate in each panel, and the black dots show the resulting temperature-density conditions that provide an acceptable match with observed abundances. The red dots represent the case where no systematic effects ( $\alpha = 1$ ) have been added. Figure adapted from [Der17].	15

Figure 6.7 The recent $^{39}\text{K}(p, \gamma)^{40}\text{Ca}$ reaction rate probability density calculation of [Lon18] as a function of temperature. The median, recommended rate is shown as the dotted normalization line. The thick and thin black lines represent the 68% ( $1\sigma$ ) and 95% ( $2\sigma$ ) uncertainty bands, respectively. The color scale shows the continuous nature of the probability density, with darker red colors closer to the recommended rate. The green line represents the previous calculation of Ref [Che81]. . . . .	17
Figure 6.8 The individual resonance contributions to the $^{39}\text{K}(p, \gamma)^{40}\text{Ca}$ reaction rate from Ref. [Lon18] as a fraction of unity. Measured resonances are represented with shading or hatched lines and are shown with their $1\sigma$ uncertainty bands. Resonances from upper limits are represented by dashed lines and show their 84% ( $+1\sigma$ ) value. The black line represents the total resonance contribution of all resonances that individually contribute less than 20% to the total reaction rate. . . . .	18
Figure 6.9 The evaporation chamber before the production of KI targets. The 3 targets shown in position become the KI #1, KI #2, and KI #3 targets after evaporation. The thickness monitor is also shown in position around a fourth opening in the 16-slot target holder. . . . .	31
Figure 6.10 A 2D histogram of the focal-plane DE vs E detector signals. Different groups correspond to different particles depending on their mass and charge. The deuteron group, highlighted in red, is being gated on in the figure. The axes have been compressed to 512 channels. . . . .	32
Figure 6.11 A histogram spectrum of the front (P1) focal-plane detector position section at $\theta_{\text{lab}} = 5^\circ$ and $E_{\text{lab}} = 21$ MeV with the KI #6 target (in red) and the carbon target (in black), both gated on the deuteron group from the the DE vs. E spectrum. Overlapping peaks indicate contaminants. . . . .	32
Figure 6.12 A 2D histogram of the front (P1) focal-plane position section vs event number over all $^{39}\text{K}({}^3\text{He}, d)^{40}\text{Ca}$ runs (#23 – #27) at $\theta_{\text{lab}} = 9^\circ$ with the KI #5 target. Both axes are compressed to 512 channels. The P1 section is zoomed in on the $^{12}\text{C}$ ground state to show the effect of energy shifts due to beam retunes. A beam retune after run #25 caused the shift in the P1 spectrum shown at event (bin) number 320. The unknown phenomenon at event (bin) number 100 occurred during run #23, which caused a reduction in counts but no energy shift. . . . .	33
Figure 6.13 A 2D histogram of the Si DE vs Si E detector signals. Different groups correspond to different particles depending on their mass and charge. The ${}^3\text{He}$ group, highlighted in red, is being gated on in the figure. . . . .	33
Figure 6.14 A 2D histogram of the Si DE vs Si total E detector signals, gated on the ${}^3\text{He}$ group and at $\theta_{\text{lab}} = 45^\circ$ . This is similar to Fig. 6.13, except the total (E+DE) Si energy has been calculated based on the slope of the peaks in the Si DE vs Si E spectrum (see Eqn. ??). Each peak is labeled with its corresponding elastic scattering element. . . . .	34

Figure 6.15 A histogram spectrum of Si Total E gated on the  $^3\text{He}$  group at  $\theta_{\text{lab}} = 45^\circ$ , obtained by projecting Fig. 6.14 onto its  $x$ -axis. Each peak is labeled with its corresponding elastic scattering element. Individual isotopes are unresolvable. . . . .

35

Figure 6.16 A Bayesian multi-gaussian fit with **BayeSpec** for the  $^{40}\text{Ca}$  excited states (in red) 6025 keV and 5903 keV from  $^{39}\text{K}(^3\text{He}, d)^{40}\text{Ca}$  and the  $^{14}\text{N}$  excited states (in orange) 5106 keV and 4915 keV from  $^{13}\text{C}(^3\text{He}, d)^{14}\text{N}$  at  $\theta_{\text{lab}} = 5^\circ$ . In red and orange are 50 random samples of the gaussian distributions from the  $\sigma$ ,  $\mu$ , and  $A$  posteriors for each peak. The  $^{40}\text{Ca}$  peaks share an identical  $\sigma$  posterior, while the  $^{14}\text{N}$  peaks share their own as well. In blue are the sums of the peaks plus the background line for each of those 50 samples. . . . .

36

Figure 6.17 The constructed priors for  $\mu - x_m$  (left) and  $A/y_m$  (right) from 10,000 samples of the  $\sigma$  and  $\lambda$  priors of Eqns. 6.11 and 6.12. The gaussian (blue) approximations were derived from the mean and standard deviation of the samples. The lognormal (red) approximations were derived from the mean and standard deviation of the natural logarithm of those samples. . . . .

36

Figure 6.18 A Bayesian exponentially-modified gaussian fit with **BayeSpec** for the 6285 keV  $^{40}\text{Ca}$  state from  $^{39}\text{K}(^3\text{He}, d)^{40}\text{Ca}$  at  $\theta_{\text{lab}} = 5^\circ$  with an oxidized potassium iodine target (KI #1). In blue are 50 random samples of the exponentially-modified gaussian distribution from the  $\sigma$ ,  $\lambda$ ,  $\mu$ , and  $A$  posteriors, plus the background line. In green are the gaussian components of the exponentially-modified gaussian samples. The new mode and peak intensity are represented by the black lines, where the solid line represents their mean and the dashed lines represent their standard deviation. . . . .

37

Figure 6.19 A Bayesian exponentially-modified gaussian fit with **BayeSpec** for the  $^{40}\text{Ca}$  excited states (left to right, in red) 7694 keV, 7658 keV, 7623 keV, and 7532 keV from  $^{39}\text{K}(^3\text{He}, d)^{40}\text{Ca}$  and the  $^{14}\text{N}$  excited state (in orange) 6446 keV from  $^{13}\text{C}(^3\text{He}, d)^{14}\text{N}$  at  $\theta_{\text{lab}} = 5^\circ$  with an oxidized potassium iodine target (KI #1). In red and orange are 50 random samples of the exponentially-modified gaussian distributions from the  $\sigma$ ,  $\lambda$ ,  $\mu$ , and  $A$  posteriors for each peak. The  $^{40}\text{Ca}$  peaks share identical  $\sigma$  and  $\lambda$  posteriors, whereas the  $^{14}\text{N}$  peak has its own. In blue are the sums of the peaks plus the background line for each of those 50 samples. . . . .

38

Figure 6.20 Differential cross-sections of unbound  $^{40}\text{Ca}$  states below 8935 keV observed in the present experiment. The left panel shows the  $l = 1$  distributions, while the right panel shows all other distributions. The experimental data were normalized to the Si detector telescope yield, as described in the text, and further scaling for illustration purposes was not necessary. The zero-range DWBA model curves were computed using the nuclear reaction code, **FRESCO** [Tho88, Tho06]. . . . .

38

Figure 6.21 Comparison between the  $^{39}\text{K}(p, \gamma)^{40}\text{Ca}$  reaction rate using the proton partial-widths and resonance energies of the present experiment (solid line, blue band) and the most recent evaluation of Ref. [Lon18] (dotted line, gray band). The reaction rate ratio is taken with respect to the median, recommended rate of Ref. [Lon18] for both calculations. The  $1\sigma$  uncertainty bands are shown. . . . .

39

Figure 6.22 Comparison between the  $^{39}\text{K}(p, \gamma)^{40}\text{Ca}$  reaction rate uncertainty using the proton partial-widths and resonance energies of the present experiment (solid band) and the most recent evaluation of Ref. [Lon18] (dotted band). Each reaction rate ratio is taken with respect to their own median, recommended rate. The  $1\sigma$  uncertainty bands are shown.

40

Figure 6.23 Individual resonance contributions to the  $^{39}\text{K}(p, \gamma)^{40}\text{Ca}$  reaction rate, where a value of 1.0 implies that the given resonance contributes 100% to the reaction rate at that temperature. The labels correspond to the energy of each resonance in keV. Resonances with shading or hatched lines have been measured and are shown with their  $1\sigma$  uncertainty bands. Resonances with a single, dashed line are upper limit calculations and show their 84% "upper"  $1\sigma$  value. The resonances displayed are those that individually account for at least 10% of the total reaction rate at their maximum. The remaining summed resonance contributions are represented by the dotted line. . . . .

41

CHAPTER

1

**INTRODUCTION**

CHAPTER

2

NUCLEAR REACTIONS  
IN STARS

## **2.1 Introduction**

## **2.2 Reaction Rates**

### **2.2.1 Wide Resonances**

### **2.2.2 Narrow Resonances**

### **2.2.3 Gamow Window**

## **2.3 Abundance Evolution**

## **2.4 Transfer Reactions**

### **2.4.1 Optical Model**

### **2.4.2 Distorted Wave Born Approximation**

### **2.4.3 Spectroscopic Factors**

### **2.4.4**

CHAPTER

**3**

**RUBIDIUM PRODUCTION IN  
MASSIVE AGB STARS**

CHAPTER

4

**EXPERIMENTAL NUCLEAR  
TECHNIQUES**

CHAPTER

5

**DATA ACQUISITION SYSTEM FOR THE  
FOCAL-PLANE DETECTOR PACKAGE**

## CHAPTER

# 6

## $^{39}\text{K}(p, \gamma)^{40}\text{Ca}$ CONSTRAINTS FOR GLOBULAR CLUSTER NGC 2419

### 6.1 Introduction

This chapter details the original research constraining hydrogen-burning conditions responsible for abundance anomalies in globular clusters. In particular, the observed potassium enrichment and magnesium depletion in red giants of the globular cluster NGC 2419 is reproduced with nuclear reaction network calculations using new nuclear physics information presented in this chapter. A new reaction rate of the key potassium-destroying reaction,  $^{39}\text{K}(p, \gamma)^{40}\text{Ca}$ , is calculated from the new proton partial-widths and resonance energies of astrophysically-important, unbound  $^{40}\text{Ca}$  states measured in the proton-transfer reaction  $^{39}\text{K}({^3\text{He}, d})^{40}\text{Ca}$ . The reaction rate is significantly constrained for  $T \lesssim 110$  MK. Monte Carlo network calculations will show new temperature-density constraints for hydrogen-burning, compared with that of the previously calculated reaction rate. Hot-bottom burning in Super-AGB stars is investigated as a polluter candidate driving the Mg–K anticorrelation in NGC 2419, as well as other abundance patterns involving potassium.

### 6.2 Globular Clusters

Globular clusters are compact conglomerates of stars associated with all types of galaxies. They are typically on the order of 1 pc to a few tens of pc in radius. They are very old,

in most cases having an age of about 10 Gyr, and they are also quite luminous, with a mean absolute visual magnitude  $M_V = -7$ . Peak globular cluster formation is thought to pre-date most stellar formation in galaxies, and they may have played a crucial role in early galaxy formation [Gra19]. In the Milky Way galaxy, they often have low metallicity and are distributed throughout the halo, the thick disk, and the bulge. These properties, while interesting in their own right, are not what have made globular clusters garner considerable interest in the last few decades.

A characteristic recently attributed to globular clusters, which distinguishes them from similar objects such as open clusters, is the presence of chemical inhomogeneities among their low-mass stars. Once labeled *abundance anomalies*, these inhomogeneities take the form of anticorrelations among the abundances of light element pairs, such as O–Na and Mg–Al. A new definition of globular clusters that includes this characteristic was suggested by Ref. [Car10], since almost every globular cluster in which abundances have been observed has exhibited an O–Na anticorrelation. The only exceptions are Terzan 7 and Pal 12, where the simultaneous Na and O abundances of only 7 [Sbo07] and 4 [Coh04] stars were observed, respectively. Other anticorrelations and correlations are exhibited in some, but not all globular clusters, making each cluster distinguishable by the combination and extent of their abundance inhomogeneities. These cluster-to-cluster differences are primarily driven by differences in luminosity and metallicity. Meanwhile, no anticorrelations have ever been observed in open clusters [Gra19].

Fig. 6.1 shows the ubiquitous O–Na anticorrelation in 1,200 red giants among all 19 globular clusters sampled by Ref. [Car10]. The red giants with an enhanced Na abundance are associated with a depletion in O abundance, and vice versa. The populations of red giants are split into 3 categories based on the extent of their Na enrichment, and associated O depletion. These populations are the primordial (P), extreme (E), and intermediate (I) components, as indicated in the first panel of Fig. 6.1. The primordial population is Na-poor/O-rich, the extreme population is Na-rich/O-poor, and the intermediate population is in-between. The primordial population is so-called because the same abundance pattern is typical of field stars with a similar metallicity. However, the Na and O abundances of the intermediate and extreme populations indicates that these red giants went through an unknown process. Low-mass stars like red giants and main sequence stars do not reach the high temperatures necessary for the nucleosynthesis chains that produce the observed Na and O abundances. This reasoning also applies to the other observed anticorrelations in globular clusters [Pra07].

The most likely scenario explaining these inhomogeneities is that the currently observed stars are part of a second generation which formed from the ashes of an older, first generation of stars. The material ejected from these more-massive first generation stars upon their death

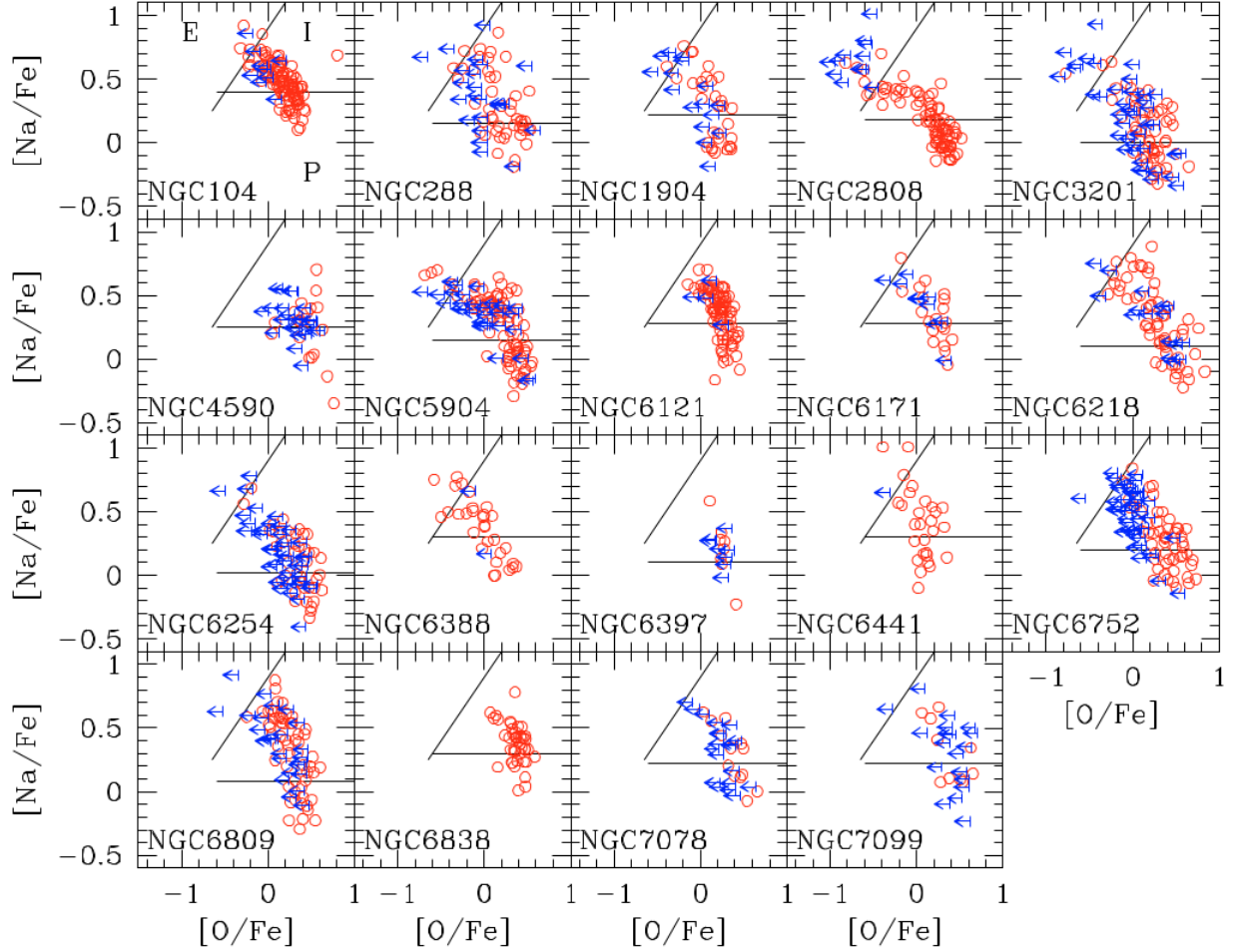


Figure 6.1: The O–Na anticorrelation of 1,200 red giants among all 19 globular clusters observed in the survey of Ref. [Car10]. Blue arrows indicate upper limits in O abundances, while lines separate different populations of red giants based on their relative O and Na richness. Primordial (P), extreme (E), and intermediate (I) populations are labeled in the first panel. See text for definitions of these populations. Adapted from [Car10].

likely polluted the inter-cluster medium where the second generation stars began to form. Hence, these first generation stars are sometimes called *polluter stars*, a class of massive, extinct stars that are the origin of the apparent abundance anomalies. Different generations of stars existing in a given globular cluster would provide evidence for *multiple stellar populations*. This premise has been widely debated over the last few decades, with most research supporting it at present [Gra04, Gra12, Gra19].

Polluter stars are likely the site of the nucleosynthesis that gives rise to the currently observed abundance patterns in globular clusters. Their exact nature is unknown, but the nucleosynthesis mechanism driving the inhomogeneities in the vast majority of globular

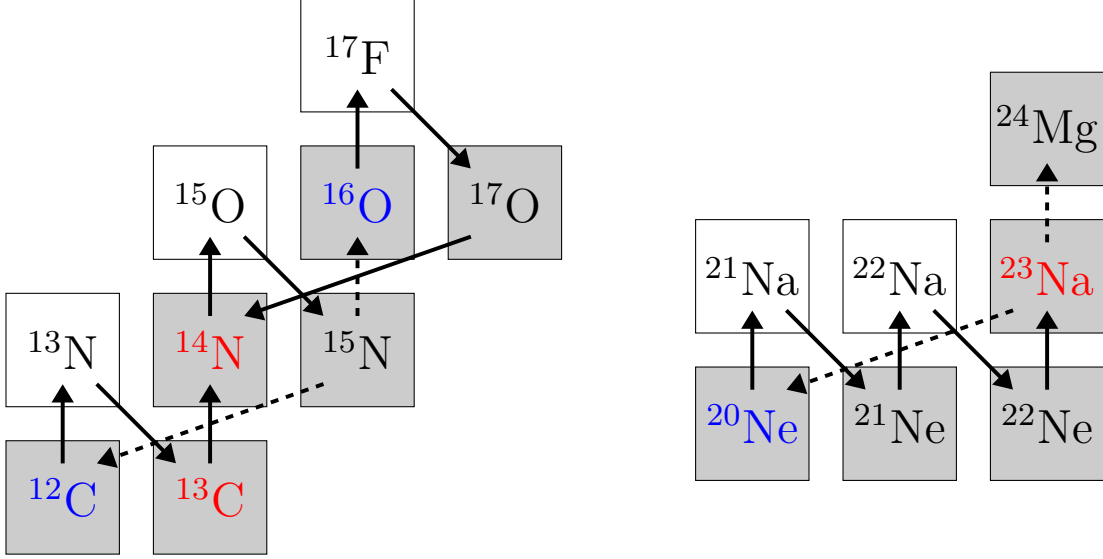


Figure 6.2: The hydrogen burning mechanism driving the O–Na anticorrelation. Nuclei in blue are destroyed overall in the various cycles, while nuclei in red are produced. Shaded nuclei are stable. The first two stages of the CNO cycle (left), distinguished by the temperature-dependent branch at  $^{15}\text{N}$ , lead to an overall depletion of oxygen. The  $^{15}\text{N}(p, \gamma)^{16}\text{O}$  reaction is activated at about 40 MK. The Ne–Na cycle (right), occurring simultaneously at about the same activation temperature, leads to an overall production of sodium. The  $^{23}\text{Na}(p, \gamma)^{24}\text{Mg}$  reaction activates at about 70 MK.

clusters is well established as proton-capture reactions in high temperature hydrogen-burning environments [Den89, Lan93]. The ubiquitous O–Na anticorrelation, for example, is exhibited in the hydrogen burning of the CNO and Ne–Na cycles at about 40 MK [Gra19]. Fig. 6.2 shows the nucleosynthesis chains that lead to an overall oxygen depletion and sodium production. The first stage of the CNO cycle involves a series of  $(p, \gamma)$  and  $(\beta^+\nu)$  reactions on stable and radioactive nuclei, respectively, starting from  $^{12}\text{C}$ . This stage occurs at fusion temperatures of about 10 MK. Once  $^{15}\text{N}$  is reached,  $^{15}\text{N}(p, \alpha)^{12}\text{C}$  will reset the cycle if the temperature is less than about 40 MK. Otherwise, the second stage of the CNO cycle will be activated from  $^{15}\text{N}(p, \gamma)^{16}\text{O}$ . This eventually leads to  $^{17}\text{O}$ , which resets the cycle via  $^{17}\text{O}(p, \alpha)^{14}\text{N}$ . This second stage leads to an overall destruction of oxygen. Meanwhile, the Ne–Na cycle activates at about 40 MK as well, starting from  $^{20}\text{Ne}(p, \gamma)^{21}\text{Na}$ . Once  $^{23}\text{Na}$  is reached, it will reset the cycle via  $^{23}\text{Na}(p, \alpha)^{20}\text{Ne}$  if temperatures are less than about 70 MK, otherwise  $^{23}\text{Na}(p, \gamma)^{24}\text{Mg}$  is activated. These destruction reactions on  $^{23}\text{Na}$  are slow enough such that sodium is produced overall.

Although nucleosynthesis via hydrogen burning is what drives the observed abundance

patterns, it is not the only mechanism responsible for them. The majority of second generation stars must be composed of a mixture of nuclear-processed ejecta and matter with a pristine composition, in order for nuclear reaction network models to reproduce the observed globular cluster abundance patterns [Pra07]. The nuclear-processed ejecta is the matter resulting from nucleosynthesis via hydrogen burning in the first generation polluter stars, while pristine matter refers to the unprocessed gas left behind from the first burst of star formation. Many polluter star sites such as AGB stars, fast-rotating massive stars, and supermassive stars require dilution with unprocessed gas in order to convert their correlated O and Na abundances into the observed anticorrelation [D'E10, D'E11, D'E12]. The observed, mixed abundances in a typical dilution model are obtained by diluting one part of processed matter with  $f$  parts of pristine matter, as in

$$X_{\text{mix}} = \frac{X_{\text{proc}} + f X_{\text{pris}}}{1 + f}, \quad (6.1)$$

where  $X$  is the mass fraction of a given nuclide among its specific composition and  $f$  is the dilution factor [Pra07, Car09]. A very small dilution factor represents nearly pure processed matter, while a very large dilution factor results in mostly pristine matter. The dilution model works very well for most globular clusters, but often a single dilution model does not simultaneously reproduce the abundances of the extreme and intermediate populations. In these cases, more than one class of polluter stars is required to match the observations, suggesting that the multiple populations premise may be more complex than previously considered [Gra19].

### 6.3 NGC 2419 and the Mg–K Anticorrelation

While the O–Na anticorrelation is ubiquitous in globular clusters, there are other abundance patterns that are unique to individual or a small subset of globular clusters. The globular cluster NGC 2419 was recently found to exhibit some puzzling abundance patterns. About 30% of the red giants observed show a strong K enrichment correlated with a considerable Mg depletion [Muc12, Coh12]. Fig. 6.3 shows the observed elemental potassium and magnesium abundances, with respect to iron, for the red giants in NGC 2419 sampled by Ref. [Muc12] in red and Ref. [Coh12] in blue. This was the first discovery of a Mg–K anticorrelation in any globular cluster. Only one other cluster to date, NGC 2808, has exhibited such an anticorrelation in a small portion of its stars [Muc15, Muc17], but the extent of the K enrichment is about 7 times less than that of NGC 2419. Meanwhile, the extent of the Mg depletion is about 3 times less. The evolutionary history of NGC 2419 must therefore be

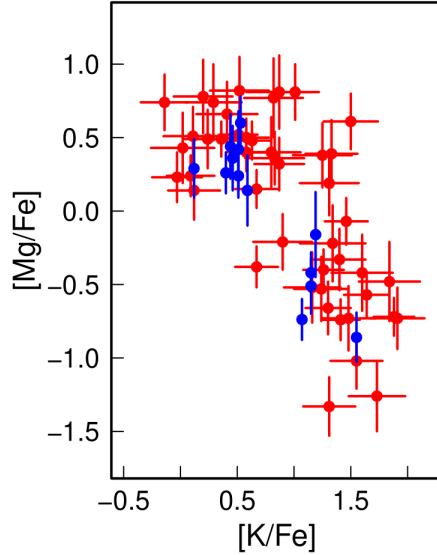


Figure 6.3: The observed Mg and K elemental abundances of red giants in NGC 2419 from Refs. [Muc12] (red) and [Coh12] (blue). Figure adapted from [Ili16].

rather unique for it to exhibit such abundance patterns not seen in other globular clusters.

Just as the nucleosynthesis mechanism for the O–Na anticorrelation involves a series of  $(p, \gamma)$  reactions and radioactive decays, the same is true for the Mg–K anticorrelation. The hydrogen burning schemes are illustrated in Fig. 6.4. The Mg–Al cycle, shown on the left-hand side of the figure, starts from  $^{24}\text{Mg}$  at about 70 MK. After the subsequent  $^{24}\text{Mg}(p, \gamma)^{25}\text{Al}$  and  $^{25}\text{Al}(\beta^+\nu)^{25}\text{Mg}$  reactions, there is a chance the  $^{26}\text{Al}^m$  isomer is populated. The isomer preferentially  $\beta^+$  decays to  $^{26}\text{Mg}$ , while the ground state  $^{26}\text{Al}^g$  preferentially captures a proton. Either scenario eventually synthesizes  $^{27}\text{Al}$ , which can repeat the cycle with  $^{27}\text{Al}(p, \alpha)^{24}\text{Mg}$  or proceed with  $^{27}\text{Al}(p, \gamma)^{28}\text{Si}$  if the temperature is more than about 80 MK. The overall effect is a depletion of magnesium and an enrichment of aluminum and silicon.

The hydrogen burning scheme for the K enrichment in NGC 2419 is illustrated on the right-hand side of Fig. 6.4. It has been shown to start from  $^{36}\text{Ar}$ , an  $\alpha$ -nucleus and the most abundant argon isotope at the low metallicities of the first stellar generation [Ven12]. Some authors [Ven12, Muc15] have incorrectly claimed that the main K enrichment chain involves the decay of  $^{37}\text{Ar}$  to  $^{37}\text{Cl}$ , then the subsequent  $^{37}\text{Cl}(p, \gamma)^{38}\text{Ar}$  reaction, indicated by the dashed arrows in Fig. 6.4. However, as Ref. [Ili16] indicates, the  $^{37}\text{Ar}(p, \gamma)^{38}\text{K}$  reaction has a much larger decay constant than the electron capture reaction  $^{37}\text{Ar}(e^-, \nu)^{37}\text{Cl}$  at the stellar densities of interest. Therefore, the main chain must proceed to  $^{38}\text{K}$  before the subsequent  $^{38}\text{K}(\beta^+\nu)^{38}\text{Ar}$  and  $^{38}\text{Ar}(p, \gamma)^{39}\text{K}$  reactions. The former chain is expected

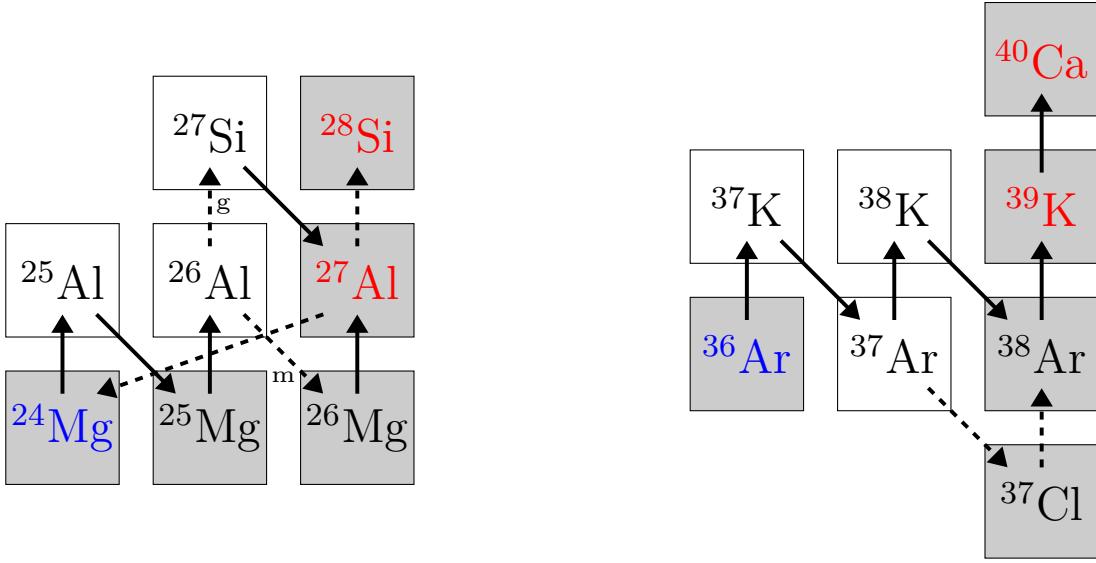


Figure 6.4: The hydrogen burning mechanism driving the Mg–K anticorrelation in the globular cluster NGC 2419. The nucleosynthesis chain for the Mg depletion is the Mg–Al cycle, shown on the left-hand side. Whether the  $^{26}\text{Al}^m$  isomer or the  $^{26}\text{Al}^g$  ground state is populated, the result is  $^{27}\text{Al}$  production, which repeats the cycle with  $^{27}\text{Al}(p, \alpha)^{24}\text{Mg}$ . The main nucleosynthesis chain for the K enrichment is shown on the right-hand side with solid arrows. The  $^{37}\text{Ar}(p, \gamma)^{38}\text{K}$  reaction proceeds at a much higher rate than  $^{37}\text{Ar}(e^-, \nu)^{37}\text{Cl}$  electron capture at the stellar densities of interest. Nuclides in blue are destroyed and nuclides in red are produced in the overall nucleosynthesis. Shaded nuclides are stable.

to contribute only marginally to  $^{39}\text{K}$  nucleosynthesis. Additionally, unlike the mechanisms for the O–Na anticorrelation and the Mg depletion, the sequence leading from  $^{36}\text{Ar}$  to  $^{39}\text{K}$  is not a cycle because the  $^{39}\text{K}(p, \alpha)^{36}\text{Ar}$  reaction has a much smaller decay constant than  $^{39}\text{K}(p, \gamma)^{40}\text{Ca}$ . However, as it will become clear in Section 6.3, the  $^{39}\text{K}(p, \gamma)^{40}\text{Ca}$  reaction rate is currently very uncertain in the astrophysical temperature range of interest.

The nucleosynthesis mechanism for the Mg–K anticorrelation may be well-established, but the site of this nucleosynthesis is much more uncertain. Ref. [Ven12] were the first to propose polluter star candidates for the Mg–K anticorrelation in NGC 2419, as well as the other observed abundance patterns. Of consideration were massive AGB stars and Super-AGB (SAGB) stars of  $\sim 6 M_\odot$ , where hydrogen burning occurs during hot-bottom burning (HBB) at the base of the convective hydrogen envelope. Agreement was found with the observed intermediate K-enriched population only in an artificially optimized scenario. The  $^{38}\text{Ar}(p, \gamma)^{39}\text{K}$  reaction rate would need to increase by a factor of 100, and the poorly known mass loss rate in the AGB models would need to simultaneously decrease by a factor

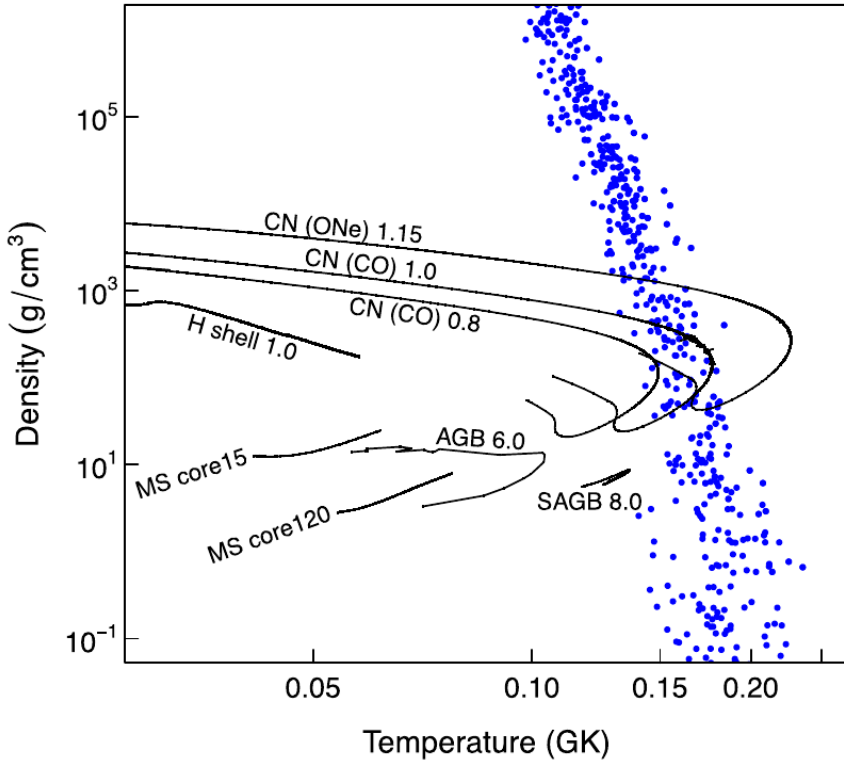


Figure 6.5: Temperature-density conditions reproducing the Mg–K anticorrelation and other abundance patterns in NGC 2419, obtained by sampling  $T$ ,  $\rho$ ,  $X_{\text{H}}$ , reaction rate probability densities, and initial abundances from a nuclear reaction network (see text). The  $T$ – $\rho$  conditions for several polluter star candidates are represented by the black lines. Adapted from Ref. [Ili16].

of 4. However, Ref. [Ven12] does not investigate the effect of varying other relevant reaction rates, which could have the same effect as increasing the  $^{38}\text{Ar}(p, \gamma)^{39}\text{K}$  rate.

Ref. [Ili16] expanded the search for polluter candidates by performing a Monte Carlo nuclear reaction network calculation that reproduced all of the observed abundances in NGC 2419, including the Mg–K anticorrelation. The parameters that were randomly sampled include the temperature  $T$ , density  $\rho$ , final hydrogen mass fraction  $X_{\text{H}}$ , all reaction rate probability densities in the network, and initial abundances. The reaction rates were obtained by truncating the Starlib [Sal13] library for the relevant rates. The resulting  $T$ – $\rho$  conditions that matched all of the observed abundances are shown by the blue dots in Fig. 6.5. A narrow band of possible  $T$ – $\rho$  conditions was found between  $\approx 80 - 260$  MK and  $\approx 10^{-4} - 10^8$  g/cm<sup>3</sup>, with additional solutions not shown in Fig. 6.5 up to 10<sup>11</sup> g/cm<sup>3</sup>. The black bands in the figure represent the  $T$ – $\rho$  hydrogen burning conditions of several polluter star candidates. These include the cores of 15 M<sub>⊙</sub> and 120 M<sub>⊙</sub> main sequence (MS) stars, the hydrogen-burning (H)

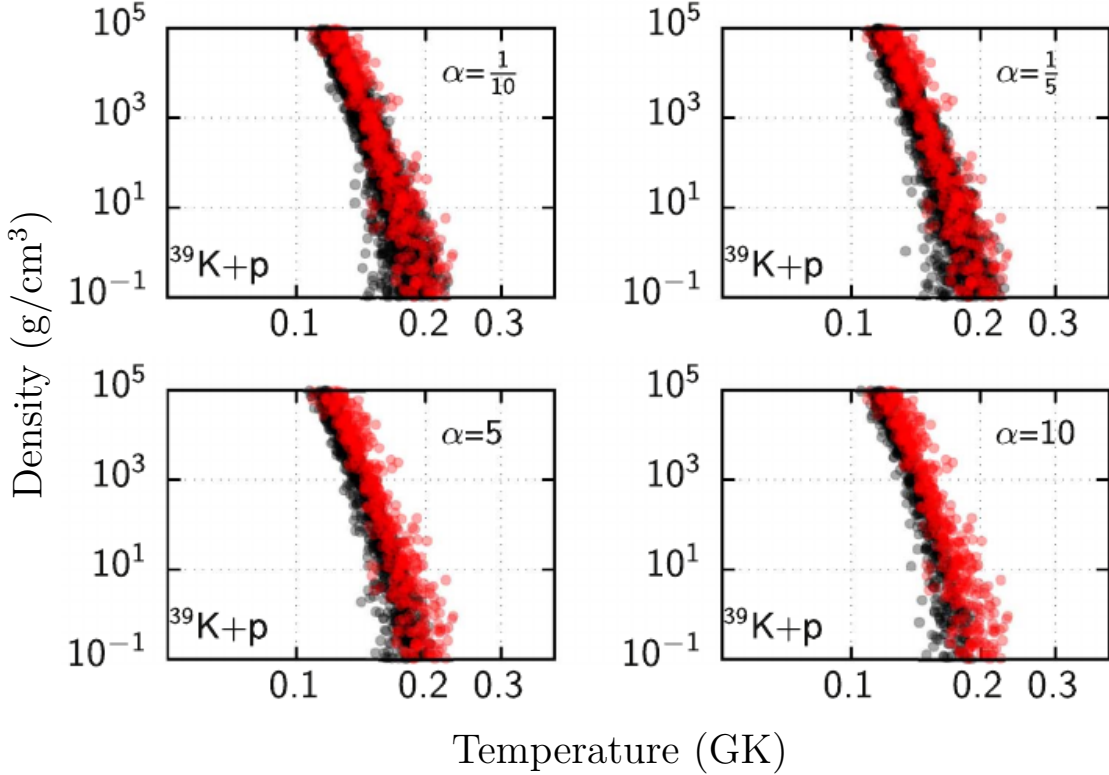


Figure 6.6: Systematic effects of the  $^{39}\text{K}(p, \gamma)^{40}\text{Ca}$  reaction rate influencing temperature-density conditions. The indicated variation factors ( $\alpha = 1/10, 1/5, 5, 10$ ) are applied to the reaction rate in each panel, and the black dots show the resulting temperature-density conditions that provide an acceptable match with observed abundances. The red dots represent the case where no systematic effects ( $\alpha = 1$ ) have been added. Figure adapted from [Der17].

shell of a  $1 M_{\odot}$  red giant star, hot-bottom burning of a  $6 M_{\odot}$  and  $8 M_{\odot}$  thermally-pulsing AGB and SAGB star, respectively, a  $1.15 M_{\odot}$  ONe classical nova, and  $0.8 M_{\odot}$  and  $1.0 M_{\odot}$  CO classical novae. The only candidates that nominally overlap with this band are ONe and CO classical novae. However, another candidate Ref. [Ili16] considers is SAGB stars because of the large uncertainty in AGB stellar model parameters, such as the mass loss rate and the prescription of convective mixing. Adjusting these parameters within their current uncertainties could increase the temperature of HBB enough to match the observed abundances.

While Ref. [Ili16] simultaneously sampled the reaction rate probability densities of all the reactions in the network, they did not investigate the effect of individual reaction rates. Ref. [Der17] investigated the sensitivity of the acceptable  $T-\rho$  conditions for NGC 2419 polluter stars on unknown systematic effects of individual reaction rates. Only 4 reactions were found to make a significant impact on the acceptable  $T-\rho$  conditions,  $^{30}\text{Si}(p, \gamma)^{31}\text{P}$ ,  $^{37}\text{Ar}(p, \gamma)^{38}\text{K}$ ,

$^{38}\text{Ar}(p, \gamma)^{39}\text{K}$ , and  $^{39}\text{K}(p, \gamma)^{40}\text{Ca}$ . If the reaction rate of  $^{39}\text{K}(p, \gamma)^{40}\text{Ca}$ , for example, were systematically larger than its recommended rate, by even as little as a factor of 5, the acceptable  $T-\rho$  band would have significantly reduced scatter and would be constrained to the low-temperature side for all densities. This scenario is shown in Fig. 6.6 on the bottom-left panel, where the black dots represent the new rate multiplied by the indicated variation factor  $\alpha$ , and the red dots represent the recommended rate ( $\alpha = 1$ ). This makes sense in theory because potassium abundance would be reduced if the rate of its primary destruction reaction were increased. The high temperature conditions would therefore destroy too much potassium compared to its observed abundance. In contrast, if the rate were systematically smaller by a factor of 5, the solutions interestingly only have increased scatter. These same effects are also true for  $^{30}\text{Si}(p, \gamma)^{31}\text{P}$ , but the opposite is true for  $^{37}\text{Ar}(p, \gamma)^{38}\text{K}$  and  $^{38}\text{Ar}(p, \gamma)^{39}\text{K}$ , as these latter reactions increase the potassium abundance.

## 6.4 The Previous $^{39}\text{K}(p, \gamma)^{40}\text{Ca}$ Reaction Rate

The remainder of this chapter will focus specifically on the key potassium-destroying reaction  $^{39}\text{K}(p, \gamma)^{40}\text{Ca}$ , found by Ref. [Der17] to be one of the few important reactions able to constrain the potassium abundance in NGC 2419 and therefore constrain the possible  $T-\rho$  conditions of its polluter stars.

### 6.4.1 Longland *et al.* (2018) Evaluation

The most recent  $^{39}\text{K}(p, \gamma)^{40}\text{Ca}$  reaction rate evaluation is that of Ref. [Lon18], which Ref. [Der17] used while it was in preparation. Its probability density was calculated using a Monte Carlo reaction rate formalism [Lon10] with resonance strengths and resonance energies provided by the direct measurements of Refs. [Kik90, Che81, Lee66]. The lowest directly measured resonance strength from these experiments is for the resonance at  $E_r^{\text{c.m.}} = 606$  keV. For resonances below this, indirect  $^{39}\text{K}({}^3\text{He}, d)^{40}\text{Ca}$  [Cag71] and  $^{39}\text{K}(d, n)^{40}\text{Ca}$  [Fuc69] proton-transfer measurements provided proton partial-widths, when available. Additionally, the indirect  $^{36}\text{Ar}({}^6\text{Li}, d)^{40}\text{Ca}$   $\alpha$ -transfer measurement of Ref. [Yam94] provided  $\alpha$ -particle partial widths for the  $(p, \alpha)$  channel, when available. Otherwise, measured or theoretical upper limits were given to the single particle reduced widths of the remaining resonances. These upper limits are described by the Porter-Thomas distribution [Por56, Wei09], truncated at the upper limit value in the case of measured upper limits. This provided a physically motivated probability density from which to sample unknown or upper-limit partial widths.

The reaction rate probability density evaluated by Ref. [Lon18] is shown in Fig. 6.7. The

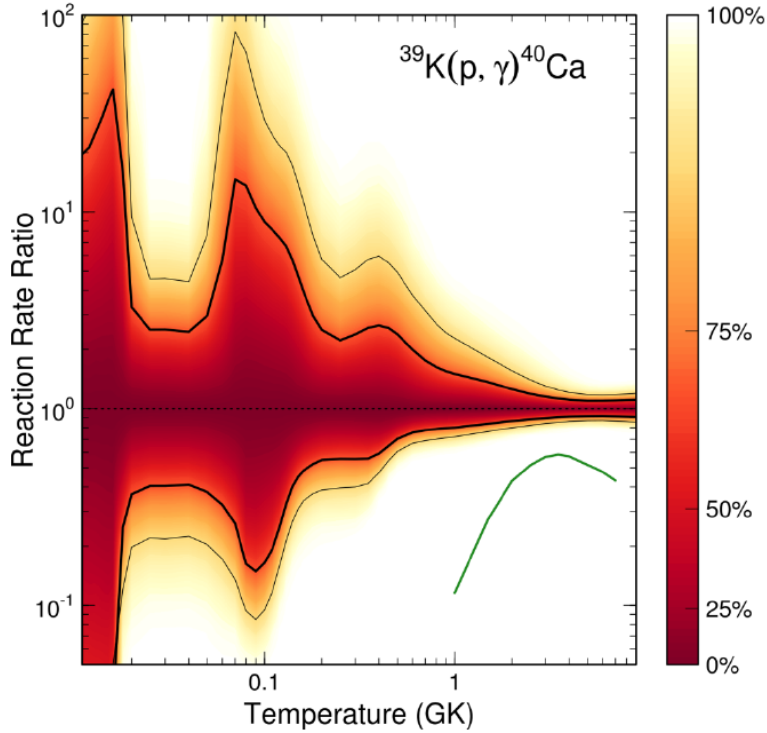


Figure 6.7: The recent  $^{39}\text{K}(p, \gamma)^{40}\text{Ca}$  reaction rate probability density calculation of [Lon18] as a function of temperature. The median, recommended rate is shown as the dotted normalization line. The thick and thin black lines represent the 68% ( $1\sigma$ ) and 95% ( $2\sigma$ ) uncertainty bands, respectively. The color scale shows the continuous nature of the probability density, with darker red colors closer to the recommended rate. The green line represents the previous calculation of Ref [Che81].

reaction rate uncertainty is represented on the  $y$ -axis as a factor of the mean, recommended rate, which has been normalized to unity. The 68% ( $1\sigma$ ) and 95% ( $2\sigma$ ) uncertainty bands are represented by the thick and thin black lines, respectively, while the color scale indicates the continuity of the probability density. Clearly, the rate uncertainty is very large between about 0.05 – 0.2 GK (50 – 200 MK), where the total  $1\sigma$  width peaks at a factor of 84 at about 80 MK. Recall from Section 6.3 that the astrophysically relevant temperature range spanning the  $T-\rho$  band in Figs. 6.5 and 6.6 is  $\approx 80 - 260$  MK. The most recent  $^{39}\text{K}(p, \gamma)^{40}\text{Ca}$  reaction rate is therefore very uncertain in the astrophysical temperature range of interest. This is concerning, given that Ref. [Der17] found that the  $T-\rho$  conditions are sensitive to systematic variations in the  $^{39}\text{K}(p, \gamma)^{40}\text{Ca}$  rate, by even as little as a factor of 5. This motivates the necessity of constraining the  $^{39}\text{K}(p, \gamma)^{40}\text{Ca}$  rate, particularly for the contributing resonances between  $\approx 50 - 260$  MK.

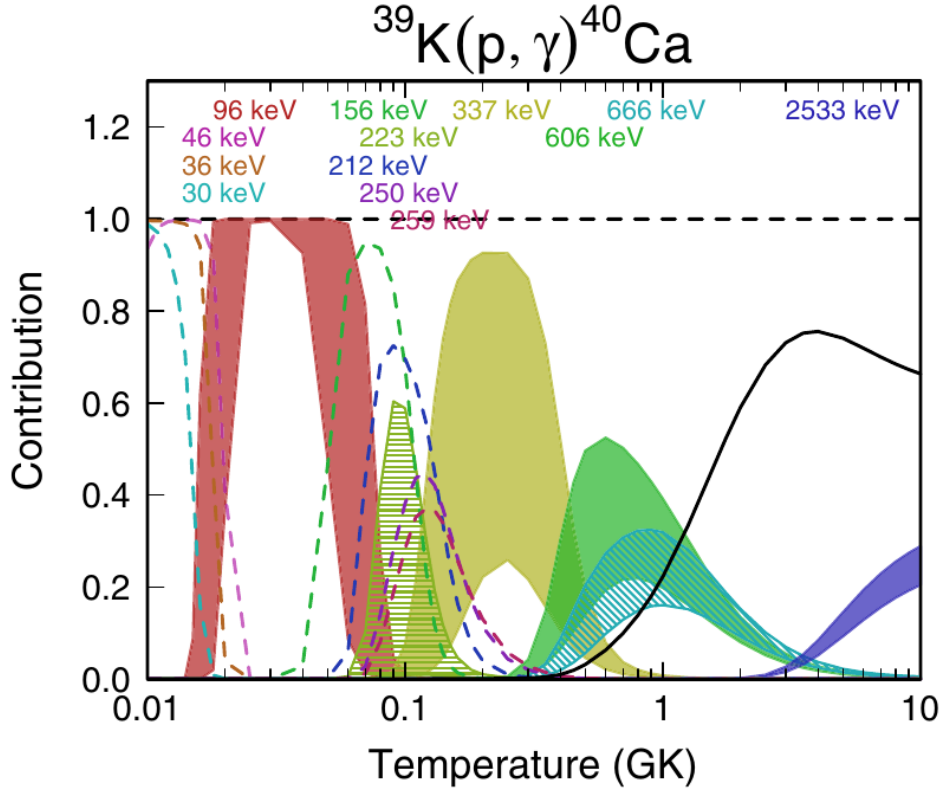


Figure 6.8: The individual resonance contributions to the  ${}^{39}\text{K}(p, \gamma){}^{40}\text{Ca}$  reaction rate from Ref. [Lon18] as a fraction of unity. Measured resonances are represented with shading or hatched lines and are shown with their  $1\sigma$  uncertainty bands. Resonances from upper limits are represented by dashed lines and show their 84% ( $+1\sigma$ ) value. The black line represents the total resonance contribution of all resonances that individually contribute less than 20% to the total reaction rate.

#### 6.4.2 Contributing Resonances

Those contributing  ${}^{39}\text{K} + p$  resonances in the  $\approx 50 - 260$  MK range span resonance energies of  $E_r^{\text{c.m.}} \approx 65 - 560$  keV (See Section 2.2.3) and  ${}^{40}\text{Ca}$  excited state energies of about  $E_x \approx 8400 - 8900$  keV, where the most recent  ${}^{40}\text{Ca}$  proton separation energy measurement is  $S_p = 8328.18(2)$  keV from Ref. [Wan21]. This resonance energy range is below the lowest directly measured resonance at  $E_r^{\text{c.m.}} = 606$  keV ( $E_x = 8935$  keV), indicating that this region is entirely described by inferred transfer reaction partial widths or upper limits at present.

The contributing resonances from the reaction rate evaluation of Ref. [Lon18] are shown in Fig. 6.8. The individual, fractional resonance contribution for each resonance is shown as a function of temperature. Measured resonances are shown with their  $1\sigma$  width, representative of the Monte Carlo formalism [Lon10] and are shaded or have hatched lines for clarity. Upper limit resonances are represented by dashed lines at their 84% ( $+1\sigma$ ) value. All resonances

that individually contribute at least 20% to the total reaction rate are shown in the figure with corresponding resonance energy labels, while the remaining resonance contributions sum to the black line. Of note are the 96 keV, 156 keV, and 337 keV resonances, which overwhelmingly contribute to the reaction rate at their respective temperatures. The 337 keV resonance, in particular, is the most important resonance between  $\approx 0.15 - 0.4$  GK (150 – 400 MK), which makes up most of the astrophysical temperature range of interest, 80 – 260 MK. However, the discrepancy between the 84% ( $+1\sigma$ ) contribution and the 16% ( $-1\sigma$ ) contribution is very large. The large uncertainty in the reaction rate around 50 – 200 MK in Fig. 6.7 is partly due to the uncertainty in this resonance contribution, but it is mostly a result of the many unknown resonances with only upper limit values between the 96 keV resonance and the 337 keV resonance.

### 6.4.3 Previous Proton-Transfer Measurements

The previous  ${}^{39}\text{K}({}^3\text{He}, d){}^{40}\text{Ca}$  [Ers66, Set67, For70, Cag71] and  ${}^{39}\text{K}(d, n){}^{40}\text{Ca}$  [Fuc69] proton-transfer measurements were not capable of achieving high resolution, particularly for unbound  ${}^{40}\text{Ca}$  states, i.e. at energies above the proton separation energy. The  $({}^3\text{He}, d)$  measurements of Refs. [Ers66, Set67, Cag71] obtained spectroscopic factors ( $C^2S$ ) for only 2 unbound  ${}^{40}\text{Ca}$  states, with ENSDF [Che17] excitation energies of  $E_x = 8425$  keV ( $E_r^{\text{c.m.}} = 96$  keV) and 8551 keV ( $E_r^{\text{c.m.}} = 223$  keV), which are both below the lowest directly measured resonance at  $E_x = 8935$  ( $E_r^{\text{c.m.}} = 606$  keV). Meanwhile, Ref. [For70] did not observe unbound  ${}^{40}\text{Ca}$  states due to their focus on lower energy excited states. The  $(d, n)$  measurement of Ref. [Fuc69] obtained  $C^2S$  for 14 unbound  ${}^{40}\text{Ca}$  states, with only 4 of these states below the lowest directly measured resonance, including 8359 keV ( $E_r^{\text{c.m.}} = 30$  keV), 8425 keV ( $E_r^{\text{c.m.}} = 96$  keV), 8551 keV ( $E_r^{\text{c.m.}} = 223$  keV), and 8665 keV ( $E_r^{\text{c.m.}} = 337$  keV). Hence, there is an overlap between the  $({}^3\text{He}, d)$  and  $(d, n)$  measurements of 2 unbound  ${}^{40}\text{Ca}$  states, 8425 keV ( $E_r^{\text{c.m.}} = 96$  keV) and 8551 keV ( $E_r^{\text{c.m.}} = 223$  keV). The  ${}^{39}\text{K}(p, \gamma){}^{40}\text{Ca}$  reaction rate calculation of Ref. [Lon18] used the  $C^2S$  measurements of Ref. [Cag71] for these 2 states, due to their more sophisticated coupled-channel DWBA calculations. They used the  $C^2S$  measurement of Ref. [Fuc69] for the 8665 keV ( $E_r^{\text{c.m.}} = 337$  keV) state. However, the reaction rate calculation did not include the 8359 keV ( $E_r^{\text{c.m.}} = 30$  keV)  $C^2S$  measurement of Ref. [Fuc69], as this state has an energy discrepancy with ENSDF [Che17] of 12 keV. This resonance was instead given an upper limit. Several unknown resonances remain below  $E_x = 8935$  keV ( $E_r^{\text{c.m.}} = 606$  keV). Ref. [Lon18] uses upper limits for 18 resonances in this region. Hence, this was strong motivation to revisit the proton-transfer reaction at modern resolution to potentially resolve the currently unknown resonances.

## 6.5 The $^{39}\text{K}(\text{He}^3, d)^{40}\text{Ca}$ Experiment

The  $^{39}\text{K}(\text{He}^3, d)^{40}\text{Ca}$  experiment was performed in 2019 over 5 days using the Enge Split-Pole Spectrograph at the Triangle Universities Nuclear Laboratory (TUNL). The 10 MV FN tandem Van de Graaff accelerator at TUNL accelerated a fully-ionized  ${}^3\text{He}$  beam to  $E_{\text{lab}} = 21$  MeV, where the energy was stabilized using a pair of high-resolution slits between two  $90^\circ$  dipole magnets (See Section ?? for experimental details). The  $^{39}\text{K}(\text{He}^3, d)^{40}\text{Ca}$  proton transfer and  $^{39}\text{K}(\text{He}^3, \text{He})^{39}\text{K}$  elastic scattering reactions were measured separately between  $\theta_{\text{lab}} = 5 - 20^\circ$  and  $\theta_{\text{lab}} = 15 - 59^\circ$ , respectively, using the focal plane detector package of Ref. [Mar19]. The  $d$  and  ${}^3\text{He}$  particles that were ejected from the target at the angle  $\theta_{\text{lab}}$  passed through the magnetic field  $B$  of the Enge Split-Pole Spectrograph, where they were then focused at a position along the focal plane, based on their magnetic rigidity  $B\rho$  (See Sec. ??). The focal-plane detector was preemptively moved via dual motors to align itself with the focal plane. Meanwhile, for every  $^{39}\text{K}(\text{He}^3, d)^{40}\text{Ca}$  or  $^{39}\text{K}(\text{He}^3, \text{He})^{39}\text{K}$  focal-plane measurement, the  $^{39}\text{K}(\text{He}^3, \text{He})^{39}\text{K}$  reaction was simultaneously measured with a silicon detector telescope inside the target chamber, positioned at a constant  $45^\circ$  from the beamline to monitor potential target degradation and other target properties.

### 6.5.1 Targets

A total of 7 natural KI (93.26%  ${}^{39}\text{K}$ , 6.73%  ${}^{41}\text{K}$ ) targets were made throughout the course of the experiment, in 2 separate evaporation batches (See Section ?? for details on the evaporation procedure). The targets labeled KI #1, KI #2, and KI #3 were made in the first batch, while those labeled KI #4, KI #5, KI #6, and KI #7 were made in the second batch, on the second day of the experiment. For each batch, the targets were simultaneously produced by evaporating approximately  $75 \mu\text{g}/\text{cm}^2$  of natural KI onto aluminum target frames, each with a  $21 \mu\text{g}/\text{cm}^2$  natural carbon (98.84%  ${}^{12}\text{C}$ , 0.96%  ${}^{13}\text{C}$ ) foil backing. The KI target thickness was measured by a thickness monitor inside the evaporation chamber, placed at roughly the same distance from the evaporation material as were the aluminum target frames with carbon backings. Fig. 6.9 shows a photograph of the chamber just before the evaporation process, with 3 natural carbon targets in position. A separate  $21 \mu\text{g}/\text{cm}^2$  natural carbon target was also used in the experiment for calibrations with the  ${}^{12}\text{C}(\text{He}^3, d){}^{13}\text{N}$ ,  ${}^{13}\text{C}(\text{He}^3, d){}^{14}\text{N}$ , and  ${}^{16}\text{O}(\text{He}^3, d){}^{17}\text{F}$  reactions, among other contaminants.

Potassium iodide is hygroscopic, meaning it will eventually oxidize at atmospheric pressure. To prevent this, care was taken to transport the targets from the evaporation chamber to the target chamber in a vacuum-sealed box at rough vacuum ( $\sim 10^{-2}$  torr), where they were then exposed to high vacuum ( $\sim 10^{-6}$  torr) for the remainder of the experiment. However, as will

be described later, the first batch of targets (KI #1, KI #2, and KI #3) oxidized at some point during the first day of the experiment, for the  $\theta_{\text{lab}} = 5^\circ$  and  $7^\circ$  ( ${}^3\text{He}, d$ ) measurements. The focal-plane spectra for these runs consisted of peaks with high-energy tails, expected of targets that undergo oxidation [Landau]. These angles were measured again toward the end of the experiment with the non-oxidized KI #6 target, but the oxidized KI #1 data was not discarded nevertheless. Section 6.6.2 details a novel technique for fitting these spectra.

### 6.5.2 Focal-Plane Spectra

The focal-plane detector package (see Section ?? and Ref. [Mar19]) consists of two position-sensitive avalanche counters, one located in the front of the detector (P1 section) and one located near the back (P2 section), a gas proportionality counter ( $\Delta E$  section), and a residual energy scintillator (E section). The data acquisition system (DAQ) triggers on the E section, located at the back of the detector, so that coincidences with all sections are established (see Section ??). The combination of the  $\Delta E$  and E sections enables particle discrimination based on mass and charge, allowing a given particle to be gated on and therefore filtering out undesired particles and detector noise in other spectra. In the  ${}^{39}\text{K}({}^3\text{He}, d){}^{40}\text{Ca}$  experiment, the  $\Delta E/E$  spectrum was used to gate on the deuteron group for  ${}^{39}\text{K}({}^3\text{He}, d){}^{40}\text{Ca}$  and the  ${}^3\text{He}$  group for  ${}^{39}\text{K}({}^3\text{He}, {}^3\text{He}){}^{39}\text{K}$ . Figure 6.10 shows an example 2D histogram of  $\Delta E$  vs E in the offline Jam software package [Jam] for the KI #6 target at  $\theta_{\text{lab}} = 5^\circ$  and an Enge magnetic field of  $B = 1.14$  T. Different particles appear in groups, with the deuteron group highlighted in red to represent a gate. Noise in the  $\Delta E$  spectrum is shown at the bottom, which is filtered out along with the other particle groups. Both the  $\Delta E$  and E signals are compressed from their original 4096 channels to 512 channels in the 2D spectrum.

The 1D histogram of the P1 section, gated on the deuteron group of Fig 6.10, is shown in Fig. 6.11 in red. The overlayed black spectrum is from a carbon target to show overlapping peaks, indicating contaminants in the KI target. The deuteron peaks shown only in red were ejected from  ${}^{39}\text{K}({}^3\text{He}, d){}^{40}\text{Ca}$  reactions in the KI target, where different excited states of the  ${}^{40}\text{Ca}$  recoil nuclei were populated, resulting in different kinematics for each deuteron depending on the excited state. Higher energy deuterons are associated with lower-energy  ${}^{40}\text{Ca}$  excited states, and vice versa. The deuterons are momentum-separated by the Enge Split-Pole Spectrograph, focusing the higher energy ones on the left side of the position sections and the lower energy ones on the right side. Thus, the P1 channel number in Fig. 6.11 is inversely related to the  ${}^{40}\text{Ca}$  excited state energies. The same is true of the recoil nuclei of the contaminants.

Table 6.1: Information on each run of the  $^{39}\text{K}(\text{He}, d)^{40}\text{Ca}$  experiment, including the angle of the Enge, the target used, the magnetic field of the Enge, and the sort group (see text).

Sort Group	$\theta_{\text{lab}}$ [°]	Run Numbers	Target	Enge Field [T]
1	5	9, 10	KI #1	1.14
2	5	11	KI #1	1.14
3	5	83 – 87	KI #6	1.14
4	7	15 – 20	KI #1	1.14
5	7	72, 75 – 78	KI #6	1.14
6	9	23	KI #5	1.145
7	9	24, 25	KI #5	1.145
8	9	26, 27	KI #5	1.145
9	11	31 – 33	KI #5	1.145
10	13	39 – 41	KI #5	1.145
11	13	42	KI #5	1.145
12	13	43, 44	KI #5	1.145
13	13	45, 47	KI #5, KI #6	1.145
14	15	55 – 59	KI #6	1.145
15	20	60, 61, 64	KI #6	1.145
16	20	65, 66	KI #6	1.145

### 6.5.3 Energy Shifts

### 6.5.4 Silicon Detector Telescope

To minimize the effects of uncertainty in the target thickness, non-uniformity in the target, and target degradation after exposure to the beam, the  $^{39}\text{K}(\text{He}, \text{He})^{39}\text{K}$  and  $^{39}\text{K}(\text{He}, d)^{40}\text{Ca}$  yields from the focal-plane detector were normalized to the simultaneous  $^{39}\text{K}(\text{He}, \text{He})^{39}\text{K}$  yield of a Si detector telescope positioned at a constant  $\theta_{\text{lab}} = 45^\circ$  inside the target chamber.

### 6.5.5 Oxidized Spectra

## 6.6 Bayesian Peak Fitting and Target Oxidation

The energy loss of light, charged particles through a medium is a statistical process. Particles with the same initial energy will traverse the same length in the medium with a distribution of final energies. This phenomenon is known as energy straggling and was theoretically described by Landau [[Landau](#)]. Thin-film targets are ideal for high resolution spectral analysis because the energy loss distribution is approximately gaussian. Thick targets, however, alter the energy loss distribution in ways that present challenges to fitting peaks in a spectrum.

Section 6.6.1 presents the Bayesian peak fitting procedure implemented in the analysis of the  $^{39}\text{K}(\text{He}, d)^{40}\text{Ca}$  experiment for the case of thin targets, and Section 6.6.2 presents a modified procedure for the case of thick targets, resulting from target oxidation which produces tails in the energy loss distribution.

### 6.6.1 Bayesian Peak Fitting

Transfer reaction analysis requires precise experimental cross section measurements for each relevant excited state of the residual nucleus. Each cross section is proportional to the yield of the transfer reaction populating the given excited state. An essential ingredient in the yield measurement, described in more detail in Section 6.7, is the number of counts of ejectile particles measured by the focal-plane detector. Each count contributes to a peak along the focal-plane spectrum corresponding to the given excited state with a finite width. The peaks are distinguished by their excitation energies, which are determined through an energy calibration based on their relative centroid positions along the focal-plane, as is done in Section 6.8.1. A typical transfer reaction spectrum will include many such peaks, as well as peaks from reactions in the target not necessarily of interest, known as contaminants. As mentioned in the introduction of this section, excited state peaks are typically gaussian-distributed, assuming a thin-film target is used. The spectrum will also include background counts, represented by a straight line. A precise determination of the number of counts in a given peak, in the simplest case, is therefore done by fitting a gaussian with a background line.

The target for the  $^{39}\text{K}(\text{He}, d)^{40}\text{Ca}$  experiment was natural potassium iodine on a natural carbon film backing. The most prominent contaminants were from  $(\text{He}, d)$  reactions on  $^{12}\text{C}$ ,  $^{13}\text{C}$ ,  $^{14}\text{N}$ , and  $^{16}\text{O}$ , producing excited states from the residual nuclei  $^{13}\text{N}$ ,  $^{14}\text{N}$ ,  $^{15}\text{O}$ , and  $^{17}\text{F}$ , respectively. The chosen magnetic field of the Enge Split-Pole Spectrograph was such that deuterons from  $(\text{He}, d)$  reactions with iodine were not at all present along the focal-plane, and deuterons from  $^{41}\text{K}(\text{He}, d)$  were only minimally present. However, given the presence of the many other contaminants, and to distinguish doublets, triplets, and other mutliplets, it was deemed necessary to use a more sophisticated technique to fit the peaks from this experiment than a simple chi-squared minimization. Bayesian Monte Carlo sampling was a natural choice, considering its realistic uncertainty handling and flexibility when dealing with non-gaussian fits, presented in Section 6.6.2. I used the **BayeSpec** [**BayeSpec**] graphical user interface (GUI), along with custom Bayesian sampling routines described below, to acquire fits to the  $^{39}\text{K}(\text{He}, d)^{40}\text{Ca}$  data.

Most peaks from transfer reactions on a thin-film target are gaussian-distributed,

$$f(x; A, \mu, \sigma) = A \exp\left(-\frac{(x - \mu)^2}{2\sigma^2}\right), \quad (6.2)$$

where  $A$  is the peak intensity,  $\mu$  is its mean, and  $\sigma$  is its standard deviation. Bayesian sampling can be used to optimize these 3 parameters to match the focal-plane data if appropriate prior distributions are known. In this case, each prior distribution is approximately normal,  $\mathcal{N}(\mu_0, \sigma_0^2)$ , with its own mean  $\mu_0$  and standard deviation  $\sigma_0$ . Posterior distributions can then be computed from these priors to achieve parameter values with statistically realistic uncertainties that match the data. These more realistic uncertainties make it possible to handle difficult fitting scenarios that would normally cause problems for chi-square minimizations, such as distinguishing peaks in a multiplet with appropriate uncertainties.

Prior means  $\mu_0$  for  $A$  and  $\mu$  are particularly simple to obtain if the peak apex is visible. Even if it is not visible, as in the case of a multiplet, a guess can be made for each peak apex location,  $(x, y)$ , based on the curvature of their sum, where  $x$  is the mean guess and  $y$  is the intensity guess. Each guess is established by selecting a point using the `BayeSpec` GUI. The prior standard deviations  $\sigma_0$  for  $A$  and  $\mu$  are given constant values conservative enough for sampling to be successful in even the most uncertain cases. These can be adjusted by the user, but are typically left as their defaults, listed below.

The prior mean  $\mu_0$  and standard deviation  $\sigma_0$  for  $\sigma$  are ideally given constant values for a given reaction representative of most peaks from that reaction in focal-plane spectra. This is because energy loss is nearly equivalent for peaks with similar excitation energies from the same reaction, but it is not equivalent for peaks from different reactions. Therefore, peaks from each reaction should ideally have a shared  $\sigma$  prior and a shared  $\sigma$  posterior in a single fit if multiple peaks are fit simultaneously. In practice, a single  $\sigma$  prior can be used for different reactions if it is conservative enough for sampling to be successful, but the  $\sigma$  posteriors should remain different for different reactions.

A background line must also be included in the model, where its intensity  $y_{bg}$  and slope  $m_{bg}$  have their own  $\mathcal{N}(\mu_0, \sigma_0^2)$  priors. Put together, the prior distributions for gaussian peaks

on a background line in a typical focal-plane spectrum are

$$\begin{aligned}
A_i &\sim \mathcal{N}(y_i, 10.0^2) \\
\mu_i &\sim \mathcal{N}(x_i, 1.0^2) \\
\sigma &\sim \mathcal{N}(5.0, 1.0^2) \\
y_{\text{bg}} &\sim \mathcal{N}(\max(1, \min(d)), 0.1^2) \\
m_{\text{bg}} &\sim \mathcal{N}(0, 0.01),
\end{aligned} \tag{6.3}$$

where  $\sigma$  is a constant prior for all reactions, but it can easily be adjusted by the user for different reactions if needed, and  $d$  refers to the focal-plane data in the specified fit range. The prior for  $m_{\text{bg}}$  can also be adjusted if the background line is clearly not horizontal. The model function to be fit is

$$f(x; A, \mu, \sigma, y_{\text{bg}}, m_{\text{bg}}) = \sum_i^N A_i \exp\left(-\frac{(x - \mu_i)^2}{2\sigma_j^2}\right) + \left(y_{\text{bg}} + m_{\text{bg}}(x - \min(x))\right), \tag{6.4}$$

where  $N$  is the total number of gaussian peaks to be fit and  $\sigma_j$  refers to the shared standard deviation for peaks from reaction  $j$ .

The posterior computation in the custom Bayesian sampling routine uses the `quap` function in R, part of the Bayesian `rethinking` package from Richard McElreath [McElreath2020]. This function finds a quadratic approximation to each full posterior distribution at its mode. It is less sophisticated than Markov Chain Monte Carlo, but its relative simplicity makes it a more efficient option to use with a GUI. The model composed of Eqns. 6.3 and 6.4 is provided to `quap`, which returns the posterior quadratic approximations with built-in uncertainties. Samples from these posteriors are then used to compute the area of each gaussian, given by  $\sqrt{2\pi} \sigma_j A_i$ , along with their uncertainties. A small number of posterior samples are also used to graphically display the gaussian fits, with different colors representing different reactions.

Figure 6.16 shows an example of this Bayesian fitting procedure for a  ${}^{39}\text{K}({}^3\text{He}, d){}^{40}\text{Ca}$  focal-plane spectrum at  $\theta_{\text{lab}} = 5^\circ$ . Excited states of  ${}^{40}\text{Ca}$  are shown in red and  ${}^{14}\text{N}$  excited state contaminants are shown in orange. In blue is the sum of the gaussians and the background line, given by Eqn. 6.4. Each gaussian, as well as the blue curve, consists of 50 individual curves that were sampled from the posteriors to represent the uncertainties. The reason it is useful to combine these 4 peaks into one fit in this example is to better resolve the 5903 keV  ${}^{40}\text{Ca}$  state in red from the 4915 keV  ${}^{14}\text{N}$  state in orange in the double gaussian on the right side of the spectrum. The addition of the 6025 keV  ${}^{40}\text{Ca}$  peak in red and the 5106 keV  ${}^{14}\text{N}$  peak in orange on the left constrains the  $\sigma$  posteriors for the double gaussian. While this may seem like a minor correction, and it is minor in the present example, it is crucial in situations

where the double gaussian or multiplet is otherwise impossible to resolve.

### 6.6.2 Fitting Peaks with Target Oxidation

Potassium iodine is hygroscopic, meaning it easily absorbs moisture from the environment. When exposed to atmospheric pressure, the salt slowly oxidizes, forming potassium carbonate and molecular iodine. This oxidation increases the thickness of thin-film targets. The probability of particles traversing the target with large final energies is decreased, introducing a high energy tail in the ejected particle spectrum. The Landau distribution describes this energy loss, but it is computationally challenging to implement. An approximation that has been found to fit oxidized-target spectra well is the exponentially-modified gaussian (EMG) distribution [Babu2016]. The power of the EMG approximation is that its area calculation is the exact same as that of a gaussian distribution,  $\sqrt{2\pi}\sigma A$ , where  $\sigma$  and  $A$  are parameters of both gaussians and EMGs, but they have slightly different definitions as it will become clear below. This makes it very simple to determine the number of counts for EMG distributions, unlike Landau distributions, where the full area integral must be calculated.

The probability density function (PDF) of an EMG distribution  $f$  is a convolution of exponential  $g$  and gaussian  $h$  PDFs,

$$\begin{aligned} f(x; \sigma, \lambda, \mu, A) &= (g * h)(x) = \int_{-\infty}^{\infty} g(x')h(x - x') dx' \\ &= \int_0^{\infty} \lambda \exp(-\lambda x') A \exp\left(-\frac{1}{2}\left(\frac{x - x' - \mu}{\sigma}\right)^2\right) dx' \\ &= A \sigma \lambda \sqrt{\frac{\pi}{2}} \exp\left(\frac{1}{2}(\sigma\lambda)^2 - (x - \mu)\lambda\right) \operatorname{erfc}\left(\frac{1}{\sqrt{2}}\left(\sigma\lambda - \frac{x - \mu}{\sigma}\right)\right), \end{aligned} \quad (6.5)$$

where  $\lambda$  is the exponential-component rate,  $\mu$ ,  $\sigma$ , and  $A$  are the gaussian-component mean, standard deviation, and peak intensity, respectively, and  $\operatorname{erfc}$  is the complimentary error function, defined as  $\operatorname{erfc} z = 1 - \operatorname{erf} z$  for the complex variable  $z$ , where  $\operatorname{erf}$  is the error function,

$$\operatorname{erf} z = \frac{2}{\sqrt{\pi}} \int_0^z \exp(-t^2) dt. \quad (6.6)$$

The standard EMG distribution, as a function of  $x$ , has a high- $x$  tail. Since the focal-plane position spectrum channel number is inversely related to energy, the EMG must be modified to have a low- $x$  tail. This is done by simply replacing  $x - \mu$  with  $\mu - x$  to reflect the standard EMG distribution about its gaussian-component mean,  $\mu$ . The following discussion of EMG distributions assumes this reflection has been performed.

Previously it was shown for non-oxidized targets that the Bayesian fitting procedure

for a gaussian peak requires gaussian mean  $\mu$  and peak intensity  $A$  priors. The means of these priors are provided by the user when selecting an estimate at the peak apex with the **BayeSpec** GUI. However, this presents a problem when extending the procedure to EMG fits. An EMG is defined by the  $\mu$  and  $A$  parameters of its gaussian component, not the mean and peak intensity of the EMG itself. To obtain reasonable priors for the  $\mu$  and  $A$  parameters, they must be derived from the attributes of the EMG peak apex, where the user selects. This apex defines the mode  $x_m$  and peak intensity  $y_m$  of the EMG, which can both be calculated by determining the coordinates where the derivative of the PDF is equal to zero. These are

$$\begin{aligned} x_m &= \mu - \sigma^2 \lambda + \sqrt{2} \sigma z, \\ y_m &= A \exp \left( -\frac{1}{2} \left( \frac{\mu - x_m}{\sigma} \right)^2 \right), \end{aligned} \quad (6.7)$$

where  $z$  is defined such that

$$\exp(z^2) \operatorname{erfc}(z) = \sqrt{\frac{2}{\pi}} \frac{1}{\sigma \lambda}, \quad (6.8)$$

which can be solved numerically. With  $x_m$  and  $y_m$  provided by the user,  $\mu$  and  $A$  become

$$\mu(\sigma, \lambda) = x_m + \sigma^2 \lambda - \sqrt{2} \sigma z, \quad (6.9)$$

$$A(\sigma, \lambda) = y_m \exp \left( \frac{1}{2} \left( \frac{\mu - x_m}{\sigma} \right)^2 \right). \quad (6.10)$$

The priors would be fully determined if  $\sigma$  and  $\lambda$ , the parameters related to the EMG width and skewness, can be constrained. Fortunately, for a given transfer reaction observed in a focal-plane spectrum, there is little variation between these properties, much like the gaussian  $\sigma$  parameter of Section 6.6.1. From a sample of EMG fits for  $^{39}\text{K}(^{3}\text{He}, d)^{40}\text{Ca}$  peaks, reasonable priors for  $\sigma$  and  $\lambda$  were determined to be

$$\sigma \sim \mathcal{N}(5.0, 1.0^2), \quad (6.11)$$

$$\lambda \sim \mathcal{N}(0.09, 0.02^2), \quad (6.12)$$

where these are also usually sufficient for other reactions. Priors for Eqns. 6.9 and 6.10 can then be constructed by sampling from Eqns. 6.11 and 6.12. The resulting prior distributions for  $\mu - x_m$  and  $A/y_m$  are shown in Figure 6.17 in black after taking 10,000 samples from Eqns. 6.11 and 6.12. The gaussian approximations (blue) were constructed from the mean and standard deviation of the  $\mu - x_m$  and  $A/y_m$  samples, while the lognormal approximations (red) were similarly constructed from the mean and standard deviation of the natural logarithm of those samples. Note that the priors are not gaussian. In fact, the prior for  $A/y_m$  is neither

gaussian nor lognormal. However, a lognormal approximation suffices for both in practice and is preferable to the actual distributions, which are either non-analytical or at least exceedingly complicated. The Bayesian quadratic approximation function, `quap`, used with `BayeSpec` requires named prior distributions, forbidding the use of non-analytical distributions. The lognormal approximations also correctly prevent negative sample values and are therefore taken as the priors for  $\mu$  and  $A$ .

As in Section 6.6.1, once the priors have been determined, the quadratic approximations to the posteriors are computed with `quap`, and the fit is constructed from samples of the EMG distribution with those posteriors. An example of this Bayesian EMG fitting method is shown in Figure 6.18, where the 6285 keV  ${}^{40}\text{Ca}$  state from  ${}^{39}\text{K}({}^3\text{He}, d){}^{40}\text{Ca}$  at  $\theta_{\text{lab}} = 5^\circ$  is fit with an EMG distribution because the potassium iodine target for this run (KI #1) had undergone oxidation. The closely-packed blue lines are 50 representative samples of the EMG posteriors, plus that of the background line, while the green lines are the corresponding gaussian components of those EMG samples with mean  $\mu$ , standard deviation  $\sigma$ , and peak intensity  $A$ . The new mode and peak intensity from Eqn 6.7, obtained by sampling from the posteriors, are shown by the black lines, where the solid line represents its mean and the dashed lines represent its standard deviation. Note that the  $(x_m, y_m)$  coordinate lies along its gaussian component, a ubiquitous property of EMG distributions. The number of counts in the EMG distribution is simply equivalent to the area of its gaussian component,  $\sqrt{2\pi} \sigma A$ , constructed by sampling from the  $\sigma$  and  $A$  posteriors.

Figure 6.19 shows how powerful this method can be for high resolution spectral analysis with an oxidized target. The same focal-plane spectrum as Figure 6.18 is shown here, but it is focused on a region with multiple peaks. The blue summed fit consists of 5 EMG distributions, shown individually by the red and orange lines, and a small, virtually horizontal background line. As before, each distribution shows 50 lines drawn from samples of the EMG posteriors. From a simple energy calibration, the red peaks were found to be  ${}^{40}\text{Ca}$  excited states with excitation energies 7694 keV, 7658 keV, 7623 keV, and 7532 keV, from left to right, and the orange peak corresponds to the  ${}^{14}\text{N}$  6446 keV excited state. Because we expect energy loss to be nearly equivalent for peaks with similar energies from the same reaction, the  $\sigma$  and  $\lambda$  width and skewness parameter posteriors are fixed between the  ${}^{40}\text{Ca}$  peaks, while the  ${}^{14}\text{N}$  peak has its own  $\sigma$  and  $\lambda$  posteriors. The custom Bayesian sampling routines for both gaussian and EMG fits can be used for a simultaneous fit of any number of peaks from up to 3 different reactions at present, and this could easily be extended to any number of reactions when the need arises.

## 6.7 Cross Section Calculations and Si Detector Normalization

### 6.7.1 Cross Sections

### 6.7.2 Si Detector Normalization

## 6.8 $^{39}\text{K}(^3\text{He}, d)^{40}\text{Ca}$ Analysis

### 6.8.1 Energy Calibrations

### 6.8.2 Cross Sections

### 6.8.3 Oxidized Targets

### 6.8.4 Spectroscopic Factors from DWBA Models

### 6.8.5 Proton Partial Widths

## 6.9 New $^{39}\text{K}(p, \gamma)^{40}\text{Ca}$ Reaction Rate

The Monte Carlo reaction rate code, `RatesMC` [Lon10, Lon23], was used to calculate a new  $^{39}\text{K}(p, \gamma)^{40}\text{Ca}$  reaction rate probability density from the partial-widths and resonance energies reported in this work. Among the states observed in this experiment, only those that do not already have a directly measured resonance strength from  $^{39}\text{K}(p, \gamma)^{40}\text{Ca}$  [Kik90, Che81, Lee66], i.e. only those below  $E_x = 8935$  keV, were modified from the most recent reaction rate evaluation of Ref. [Lon18]. The new reaction rate is compared with that of Ref. [Lon18] in Fig. 6.21. The solid line and blue band represent the median, recommended rate and the  $1\sigma$  confidence interval of this work, respectively. The dotted line and gray band represent that of Ref. [Lon18], except with resonance energies calculated using  $S_p = 8328.18(2)$  keV from Ref. [Wan21] for consistency, but with marginal effect. Both reaction rates are normalized to the median, recommended rate of Ref. [Lon18].

As mentioned previously, the large uncertainty in Ref. [Lon18], between about 50 MK and 200 MK, corresponds to most of the relevant temperatures that reproduce the Mg–K anticorrelation in the globular cluster NGC 2419 [Ili16]. Fig. 6.21 illustrates that the new reaction rate increases significantly in this range, particularly at 70 MK where the median rate is a factor of 13 larger than the rate of Ref. [Lon18]. The  $1\sigma$  width is also significantly

reduced in this region, from a factor of 84 at 80 MK to just a factor of 2, a reduction of a factor of 42.

Our new determination of  $(2J + 1)\Gamma_p$  for the 154 keV resonance is primarily responsible for the increase in the rate and decrease in the uncertainty between about 55 MK and 110 MK. Similar effects occur between about 20 MK and 55 MK, primarily from our  $l = 1 + 3$  assignment of the 96 keV resonance, which has replaced the  $l = 3$  assignment by the other  $(^3\text{He}, d)$  measurements in this calculation. The  $(d, n)$  measurement of Ref. [Fuc69] is in agreement with the  $l = 1 + 3$  assignment for this resonance. Note that using the previous  $l = 3$  assignment has a negligible effect on the results mentioned above at 70 and 80 MK. Our  $(2J + 1)\Gamma_p$  determination for the 29 keV resonance is responsible for the rate increase below 20 MK. The smaller effects above 110 MK are from a combination of the 335 keV, 415 keV, 439 keV, and 521 keV resonances, the latter three of which have replaced  $(2J + 1)\Gamma_p$  upper limits in Ref. [Lon18].

## 6.10 Potassium Abundance in Reaction Network Calculations

## 6.11 Conclusions



Figure 6.9: The evaporation chamber before the production of KI targets. The 3 targets shown in position become the KI #1, KI #2, and KI #3 targets after evaporation. The thickness monitor is also shown in position around a fourth opening in the 16-slot target holder.

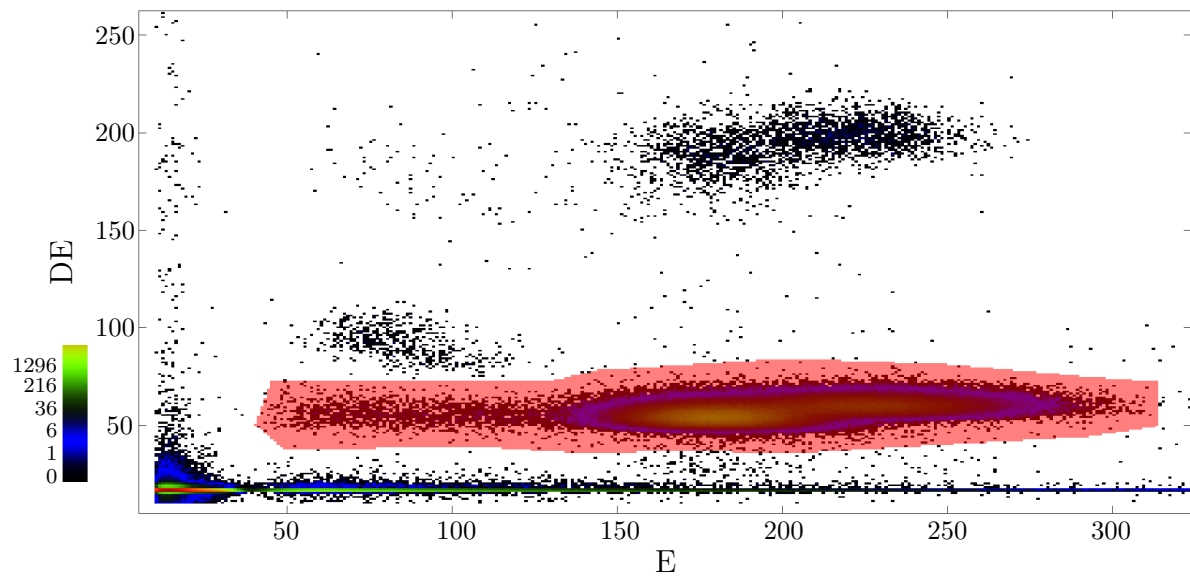


Figure 6.10: A 2D histogram of the focal-plane DE vs E detector signals. Different groups correspond to different particles depending on their mass and charge. The deuteron group, highlighted in red, is being gated on in the figure. The axes have been compressed to 512 channels.

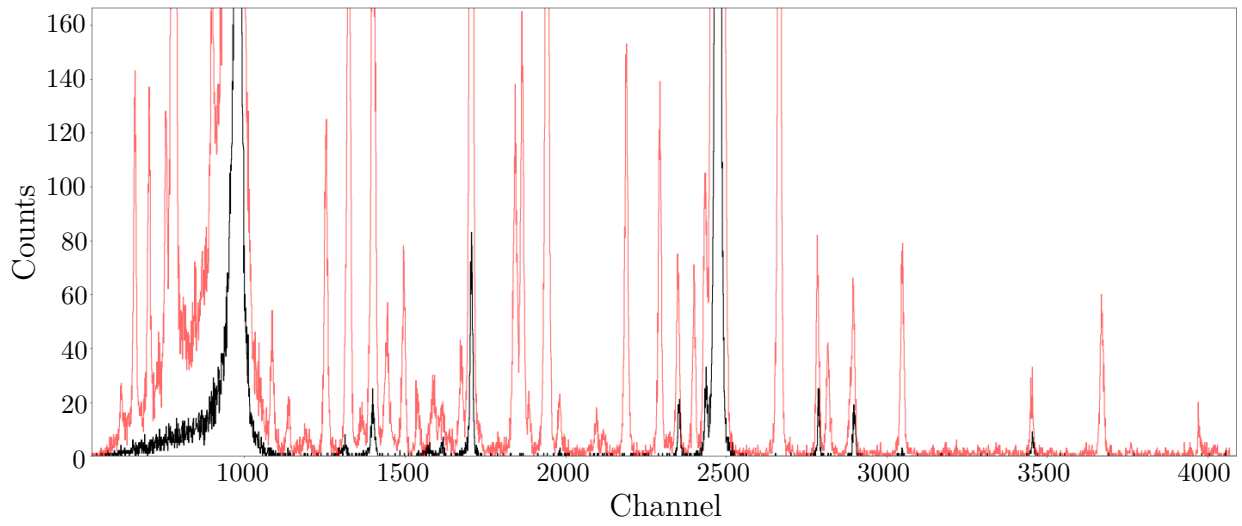


Figure 6.11: A histogram spectrum of the front (P1) focal-plane detector position section at  $\theta_{\text{lab}} = 5^\circ$  and  $E_{\text{lab}} = 21$  MeV with the KI #6 target (in red) and the carbon target (in black), both gated on the deuteron group from the the DE vs. E spectrum. Overlapping peaks indicate contaminants.

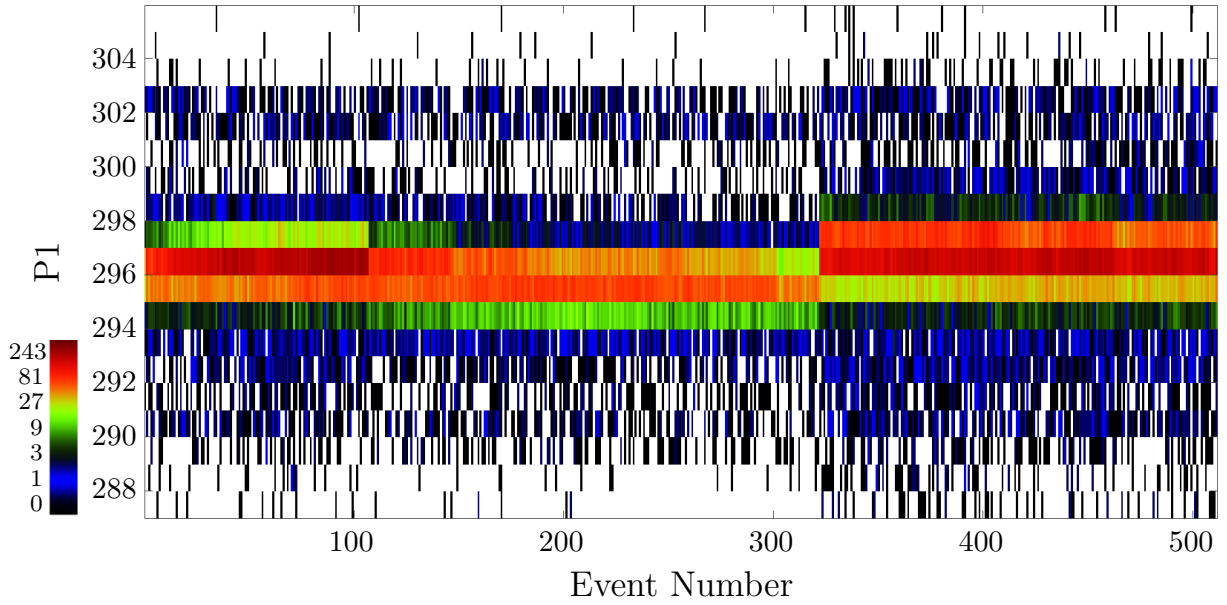


Figure 6.12: A 2D histogram of the front (P1) focal-plane position section vs event number over all  $^{39}\text{K}(^3\text{He}, d)^{40}\text{Ca}$  runs (#23 – #27) at  $\theta_{\text{lab}} = 9^\circ$  with the KI #5 target. Both axes are compressed to 512 channels. The P1 section is zoomed in on the  $^{12}\text{C}$  ground state to show the effect of energy shifts due to beam retunes. A beam retune after run #25 caused the shift in the P1 spectrum shown at event (bin) number 320. The unknown phenomenon at event (bin) number 100 occurred during run #23, which caused a reduction in counts but no energy shift.

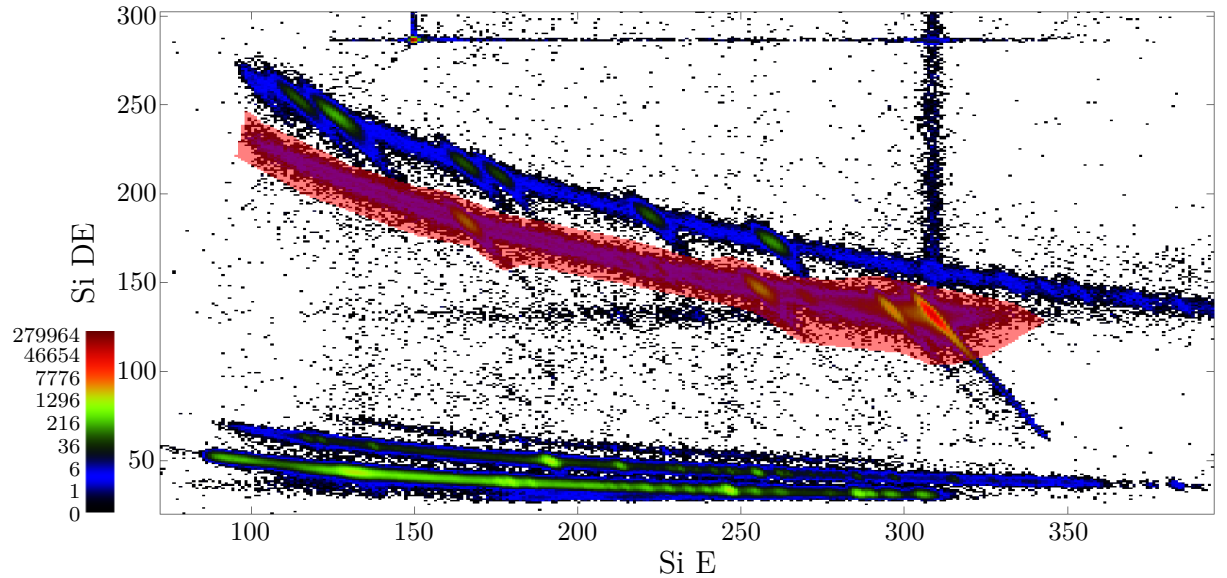


Figure 6.13: A 2D histogram of the Si DE vs Si E detector signals. Different groups correspond to different particles depending on their mass and charge. The  $^3\text{He}$  group, highlighted in red, is being gated on in the figure.

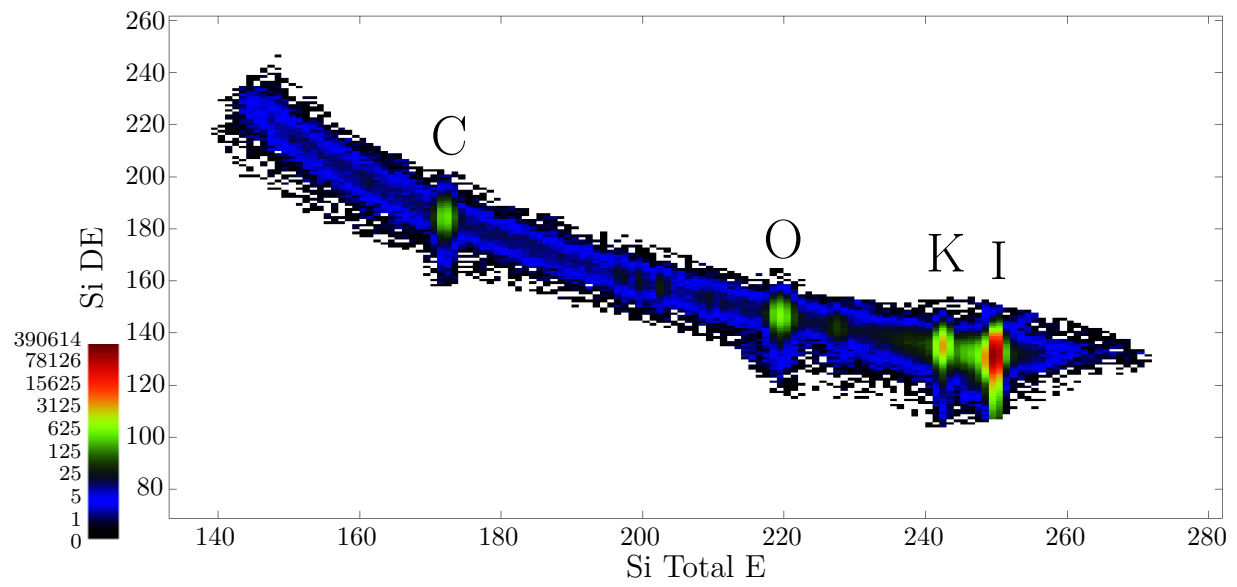


Figure 6.14: A 2D histogram of the Si DE vs Si total E detector signals, gated on the  ${}^3\text{He}$  group and at  $\theta_{\text{lab}} = 45^\circ$ . This is similar to Fig. 6.13, except the total (E+DE) Si energy has been calculated based on the slope of the peaks in the Si DE vs Si E spectrum (see Eqn. ??). Each peak is labeled with its corresponding elastic scattering element.

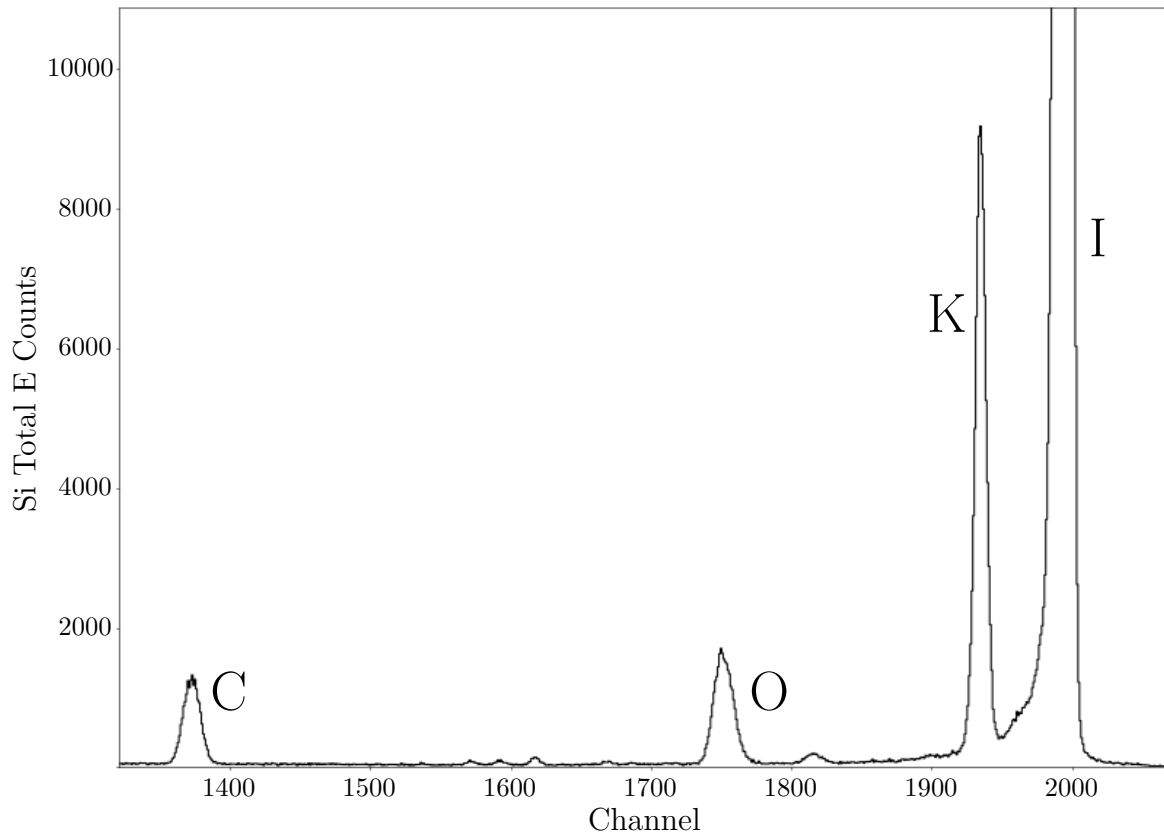


Figure 6.15: A histogram spectrum of Si Total E gated on the  ${}^3\text{He}$  group at  $\theta_{\text{lab}} = 45^\circ$ , obtained by projecting Fig. 6.14 onto its  $x$ -axis. Each peak is labeled with its corresponding elastic scattering element. Individual isotopes are unresolvable.

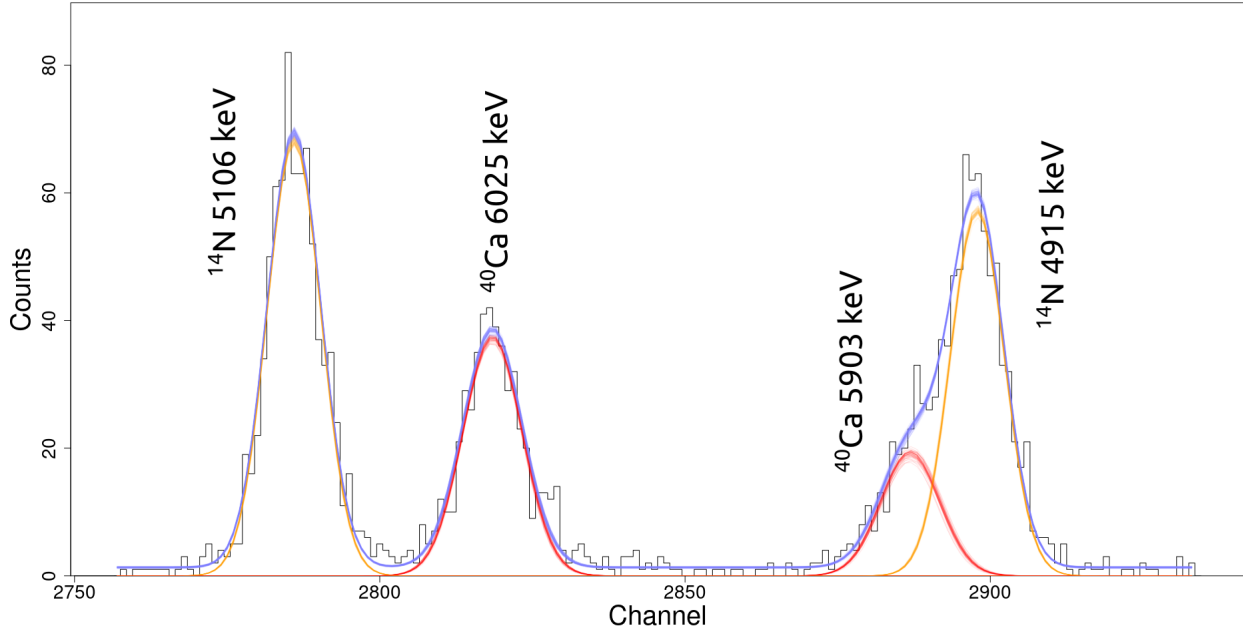


Figure 6.16: A Bayesian multi-gaussian fit with BayeSpec for the  $^{40}\text{Ca}$  excited states (in red) 6025 keV and 5903 keV from  $^{39}\text{K}(\text{He}, d)^{40}\text{Ca}$  and the  $^{14}\text{N}$  excited states (in orange) 5106 keV and 4915 keV from  $^{13}\text{C}(\text{He}, d)^{14}\text{N}$  at  $\theta_{\text{lab}} = 5^\circ$ . In red and orange are 50 random samples of the gaussian distributions from the  $\sigma$ ,  $\mu$ , and  $A$  posteriors for each peak. The  $^{40}\text{Ca}$  peaks share an identical  $\sigma$  posterior, while the  $^{14}\text{N}$  peaks share their own as well. In blue are the sums of the peaks plus the background line for each of those 50 samples.

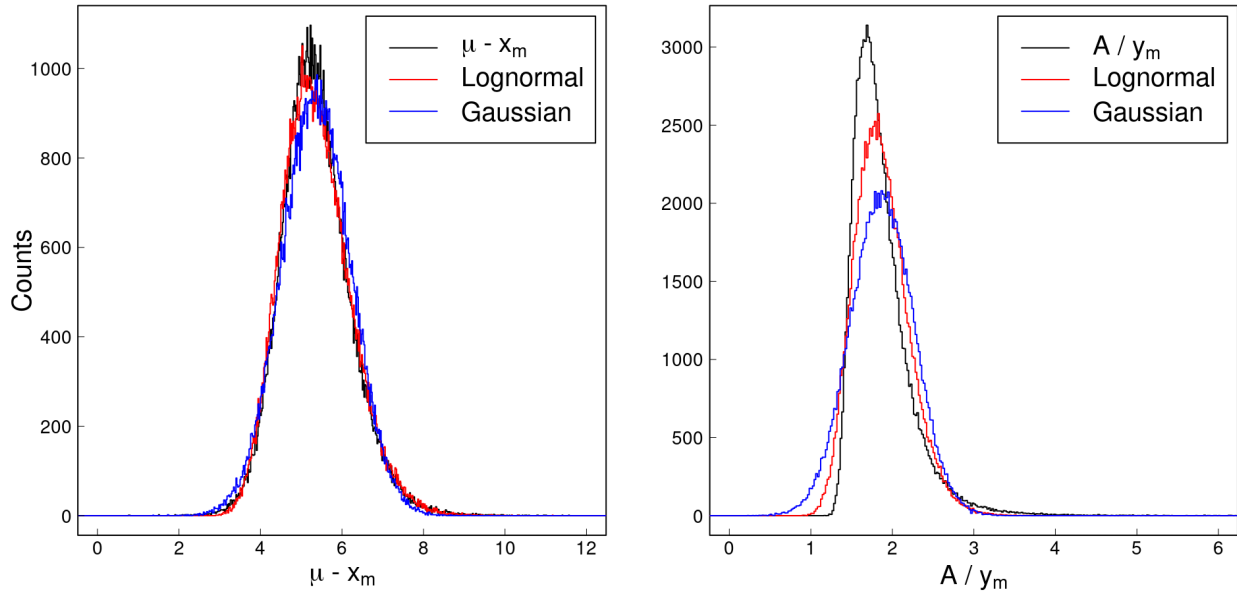


Figure 6.17: The constructed priors for  $\mu - x_m$  (left) and  $A/y_m$  (right) from 10,000 samples of the  $\sigma$  and  $\lambda$  priors of Eqns. 6.11 and 6.12. The gaussian (blue) approximations were derived from the mean and standard deviation of the samples. The lognormal (red) approximations were derived from the mean and standard deviation of the natural logarithm of those samples.

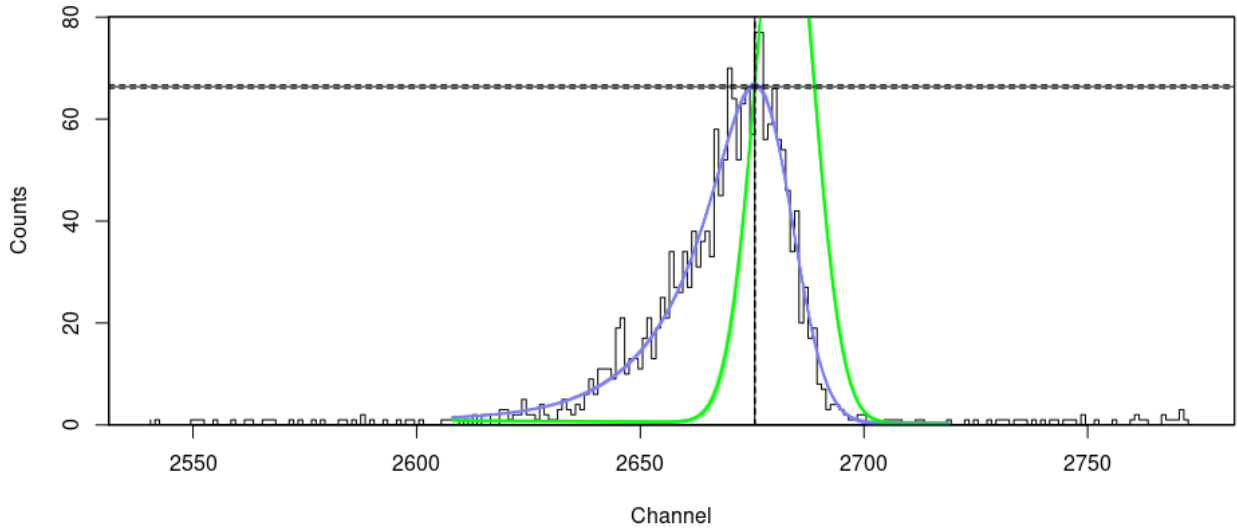


Figure 6.18: A Bayesian exponentially-modified gaussian fit with BayeSpec for the 6285 keV  $^{40}\text{Ca}$  state from  $^{39}\text{K}({}^3\text{He}, d)^{40}\text{Ca}$  at  $\theta_{\text{lab}} = 5^\circ$  with an oxidized potassium iodine target (KI #1). In blue are 50 random samples of the exponentially-modified gaussian distribution from the  $\sigma$ ,  $\lambda$ ,  $\mu$ , and  $A$  posteriors, plus the background line. In green are the gaussian components of the exponentially-modified gaussian samples. The new mode and peak intensity are represented by the black lines, where the solid line represents their mean and the dashed lines represent their standard deviation.

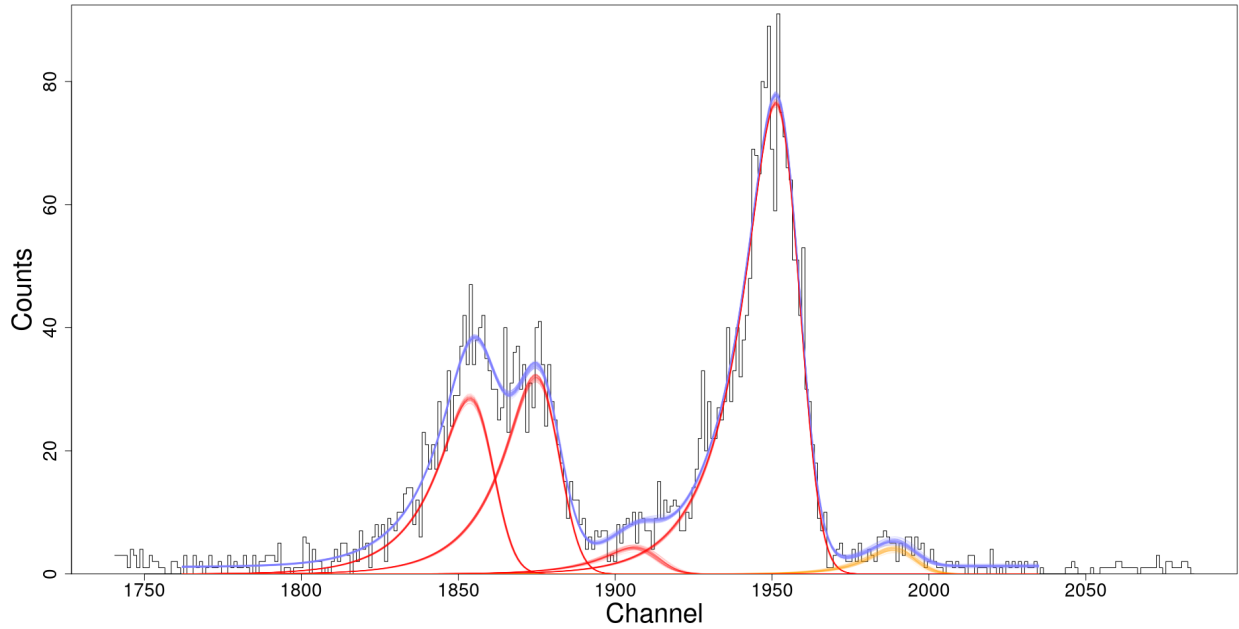


Figure 6.19: A Bayesian exponentially-modified gaussian fit with BayeSpec for the  $^{40}\text{Ca}$  excited states (left to right, in red) 7694 keV, 7658 keV, 7623 keV, and 7532 keV from  $^{39}\text{K}({^3\text{He}}, d)^{40}\text{Ca}$  and the  $^{14}\text{N}$  excited state (in orange) 6446 keV from  $^{13}\text{C}({^3\text{He}}, d)^{14}\text{N}$  at  $\theta_{\text{lab}} = 5^\circ$  with an oxidized potassium iodine target (KI #1). In red and orange are 50 random samples of the exponentially-modified gaussian distributions from the  $\sigma$ ,  $\lambda$ ,  $\mu$ , and  $A$  posteriors for each peak. The  $^{40}\text{Ca}$  peaks share identical  $\sigma$  and  $\lambda$  posteriors, whereas the  $^{14}\text{N}$  peak has its own. In blue are the sums of the peaks plus the background line for each of those 50 samples.

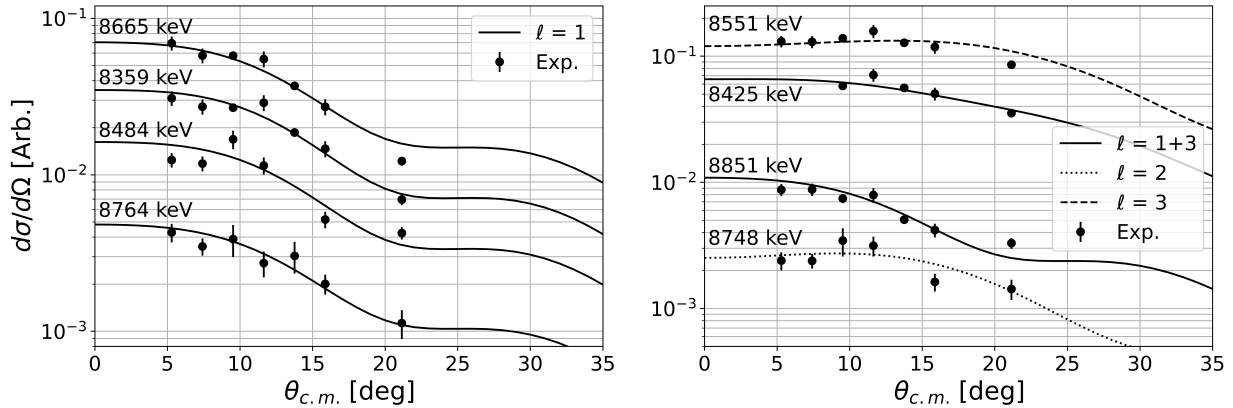


Figure 6.20: Differential cross-sections of unbound  $^{40}\text{Ca}$  states below 8935 keV observed in the present experiment. The left panel shows the  $l = 1$  distributions, while the right panel shows all other distributions. The experimental data were normalized to the Si detector telescope yield, as described in the text, and further scaling for illustration purposes was not necessary. The zero-range DWBA model curves were computed using the nuclear reaction code, FRESCO [Tho88, Tho06].

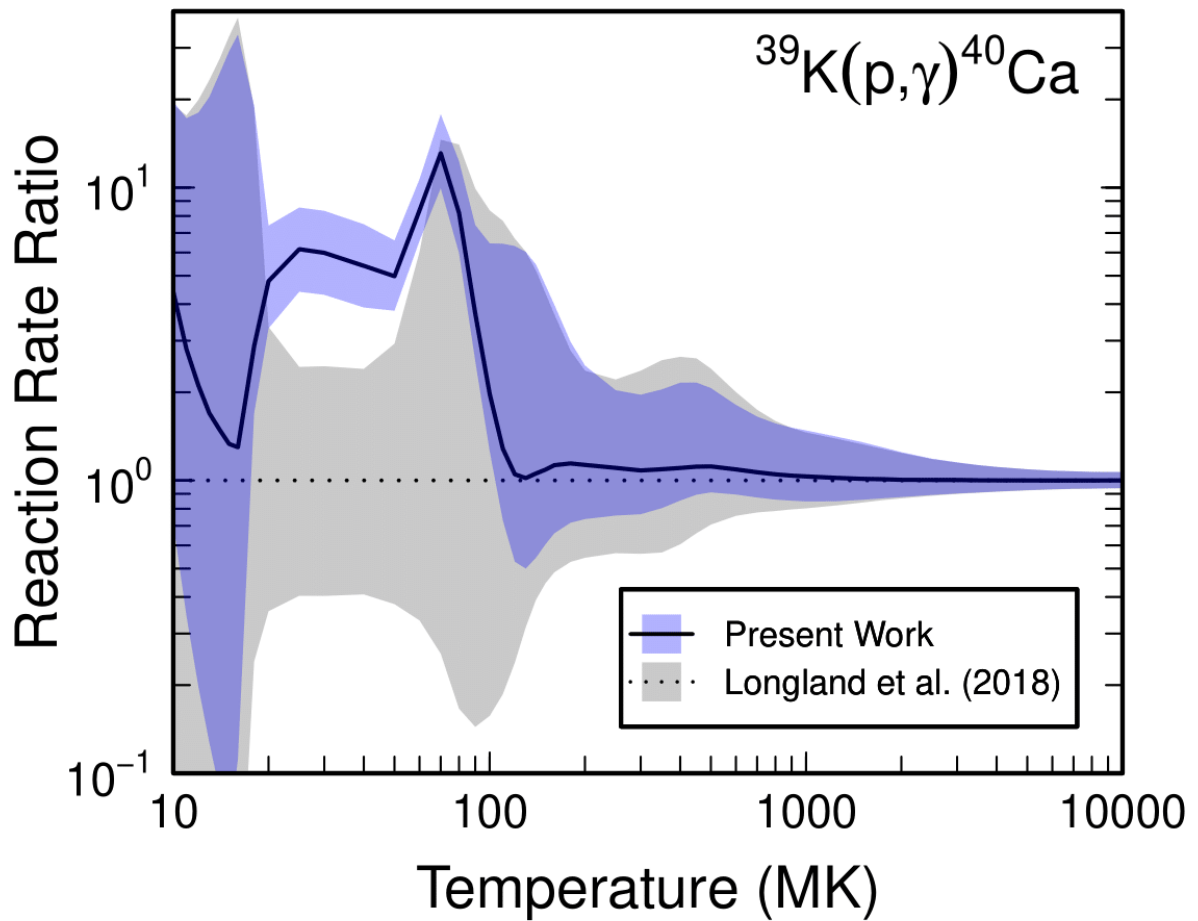


Figure 6.21: Comparison between the  $^{39}\text{K}(\text{p},\gamma)^{40}\text{Ca}$  reaction rate using the proton partial-widths and resonance energies of the present experiment (solid line, blue band) and the most recent evaluation of Ref. [Lon18] (dotted line, gray band). The reaction rate ratio is taken with respect to the median, recommended rate of Ref. [Lon18] for both calculations. The  $1\sigma$  uncertainty bands are shown.

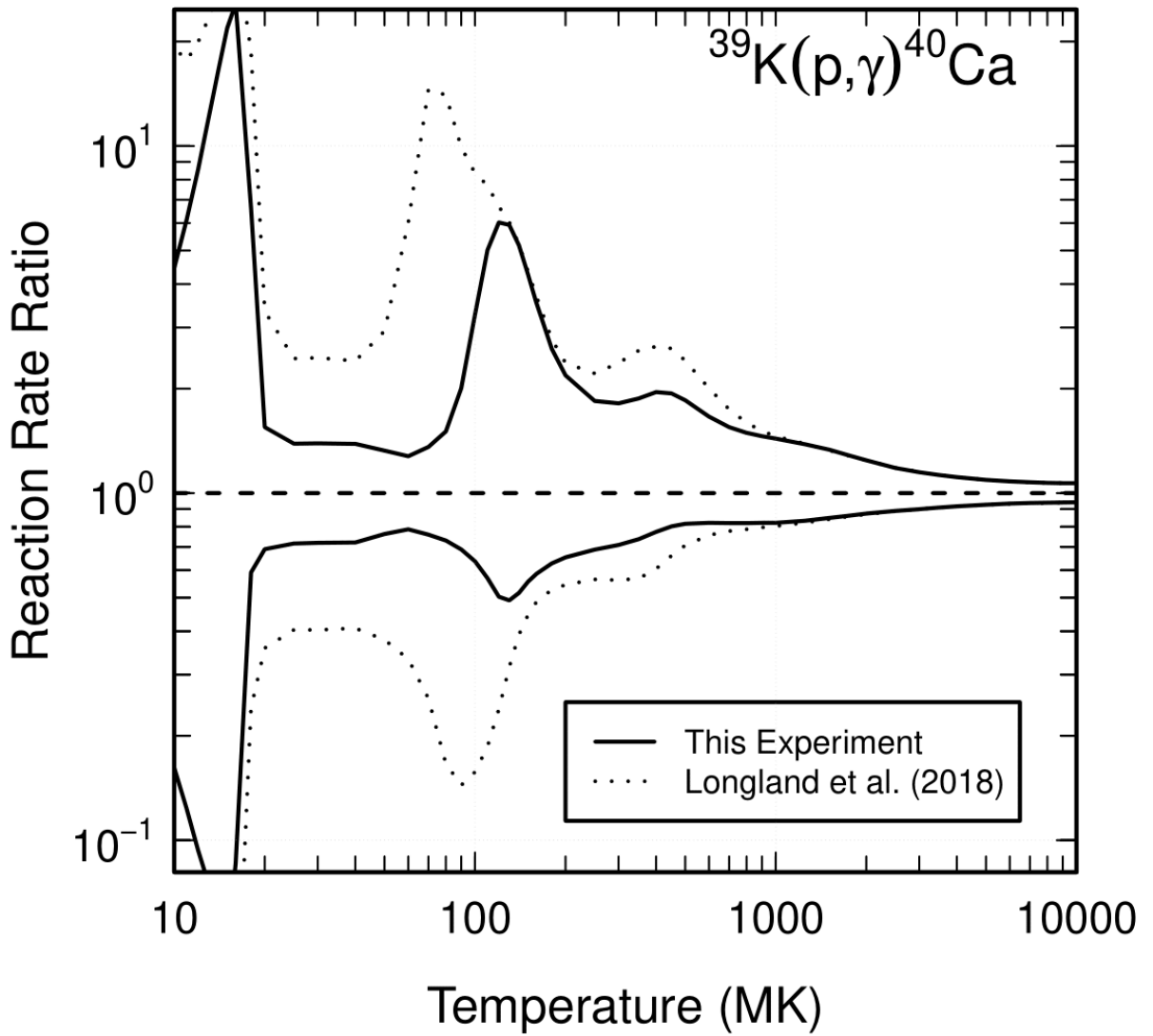


Figure 6.22: Comparison between the  $^{39}\text{K}(p, \gamma)^{40}\text{Ca}$  reaction rate uncertainty using the proton partial-widths and resonance energies of the present experiment (solid band) and the most recent evaluation of Ref. [Lon18] (dotted band). Each reaction rate ratio is taken with respect to their own median, recommended rate. The  $1\sigma$  uncertainty bands are shown.

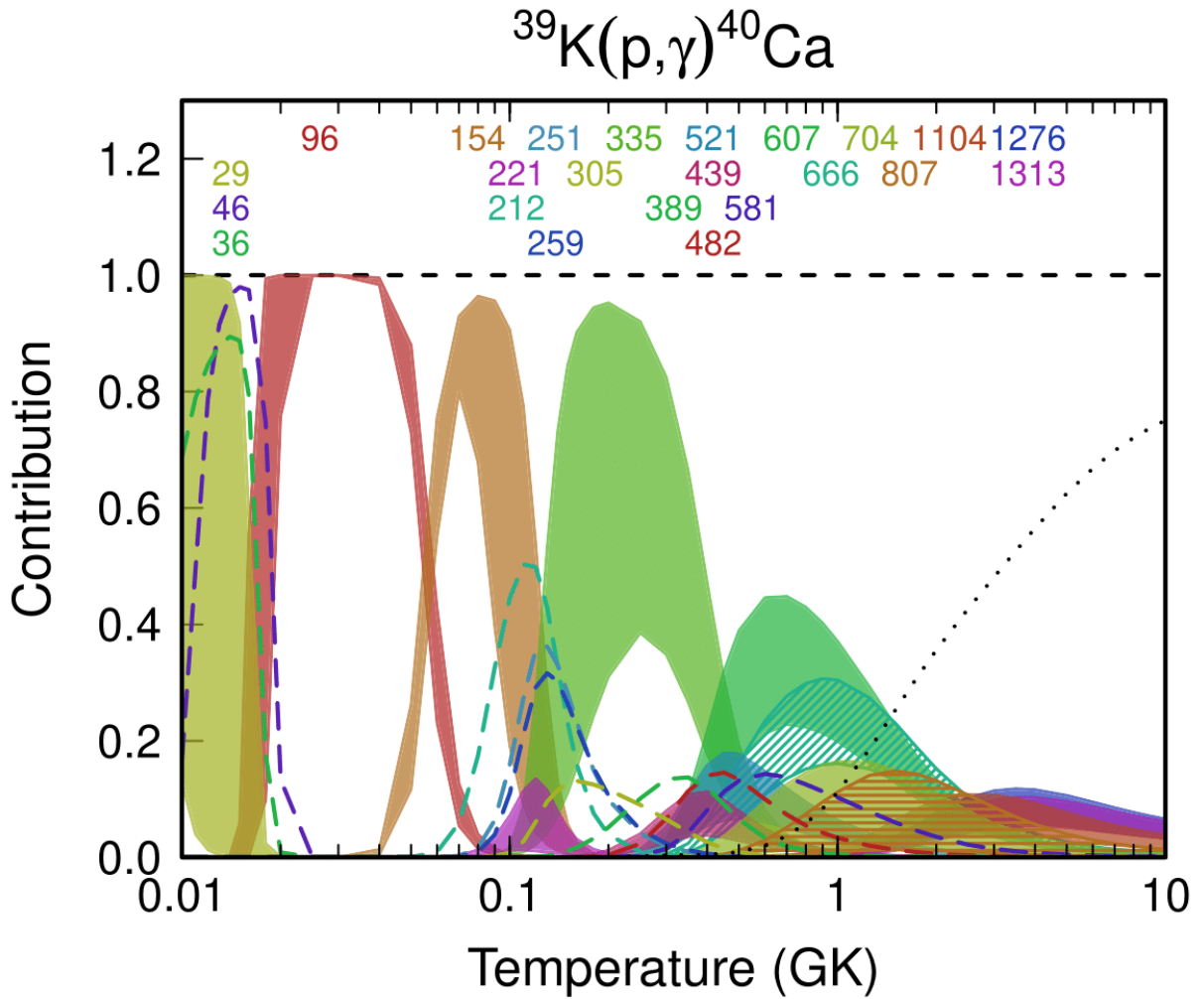


Figure 6.23: Individual resonance contributions to the  $^{39}\text{K}(p,\gamma)^{40}\text{Ca}$  reaction rate, where a value of 1.0 implies that the given resonance contributes 100% to the reaction rate at that temperature. The labels correspond to the energy of each resonance in keV. Resonances with shading or hatched lines have been measured and are shown with their  $1\sigma$  uncertainty bands. Resonances with a single, dashed line are upper limit calculations and show their 84% "upper"  $1\sigma$  value. The resonances displayed are those that individually account for at least 10% of the total reaction rate at their maximum. The remaining summed resonance contributions are represented by the dotted line.

CHAPTER

7

**SUMMARY AND CONCLUSIONS**

## BIBLIOGRAPHY

- [Cag71] M.E. Cage et al. “The  $^{39}\text{K}(^3\text{He}, ^3\text{He})^{39}\text{K}$  and  $^{39}\text{K}(^3\text{He}, d)^{40}\text{Ca}$  reactions at 29.3 MeV”. *Nuclear Physics A* **162**, 3 (1971), pp. 657–672.
- [Car09] Carretta, E. et al. “Na-O anticorrelation and HB\*\*\* - VIII. Proton-capture elements and metallicities in 17 globular clusters from UVES spectra”. *A&A* **505**, 1 (2009), pp. 139–155.
- [Car10] Carretta, E. et al. “Properties of stellar generations in globular clusters and relations with global parameters”. *A&A* **516** (2010), A55.
- [Che17] Jun Chen. “Nuclear Data Sheets for A=40”. *Nuclear Data Sheets* **140** (2017), pp. 1–376.
- [Che81] C.-W. Cheng et al. “Hydrogen burning of  $^{39}\text{K}$  in explosive oxygen burning”. *Canadian Journal of Physics* **59**, 2 (1981), pp. 238–243.
- [Coh04] Judith G. Cohen. “Palomar 12 as a Part of the Sagittarius Stream: The Evidence from Abundance Ratios\*”. *The Astronomical Journal* **127**, 3 (2004), p. 1545.
- [Coh12] Judith G. Cohen and Evan N. Kirby. “The Bizarre Chemical Inventory of NGC 2419, An Extreme Outer Halo Globular Cluster”. *The Astrophysical Journal* **760**, 86 (2012), p. 15.
- [D'E10] Annibale D'Ercole et al. “Abundance patterns of multiple populations in globular clusters: a chemical evolution model based on yields from AGB ejecta”. *Monthly Notices of the Royal Astronomical Society* **407**, 2 (2010), pp. 854–869.
- [D'E11] Annibale D'Ercole, Francesca D'Antona, and Enrico Vesperini. “Formation of multiple populations in globular clusters: constraints on the dilution by pristine gas”. *Monthly Notices of the Royal Astronomical Society* **415**, 2 (2011), pp. 1304–1309.
- [D'E12] Annibale D'Ercole et al. “The role of super-asymptotic giant branch ejecta in the abundance patterns of multiple populations in globular clusters”. *Monthly Notices of the Royal Astronomical Society* **423**, 2 (2012), pp. 1521–1533.
- [Den89] P. A. Denisenkov and S. N. Denisenkova. “Possible Explanation of the Correlation Between Nitrogen and Sodium Over Abundances for Red Giants in Globular Clusters”. *Astronomiceskij Tsirkulyar* **1538** (1989), p. 11.

- [Der17] J. R. Dermigny and C. Iliadis. “Sensitivity to Thermonuclear Reaction Rates in Modeling the Abundance Anomalies of NGC 2419”. *The Astrophysical Journal* **848**, 1 (2017), p. 14.
- [Ers66] John R. Erskine. “Energy-Level Structure of  $^{40}\text{Ca}$  as Observed with the  $^{39}\text{K}({}^3\text{He}, d)^{40}\text{Ca}$  Reaction”. *Phys. Rev.* **149** (3 1966), pp. 854–862.
- [For70] J.S. Forster et al. “Proton stripping to particle-hole states in  $^{40}\text{Ca}$  and  $^{42}\text{Ca}$ ”. *Nuclear Physics A* **150**, 1 (1970), pp. 30–48.
- [Fuc69] H. Fuchs, K. Grabisch, and G. Röschert. “Investigation of states in  $^{40}\text{Ca}$  by the  $^{39}\text{K}(d, n)$  reaction”. *Nuclear Physics A* **129**, 3 (1969), pp. 545–570.
- [Gra04] Raffaele Gratton, Christopher Sneden, and Eugenio Carretta. “Abundance Variations within Globular Clusters”. *Annual Review of Astronomy and Astrophysics* **42**, 1 (2004), pp. 385–440.
- [Gra12] Raffaele G. Gratton, Eugenio Carretta, and Angela Bragaglia. “Multiple populations in globular clusters”. *The Astronomy and Astrophysics Review* **20**, 1 (2012), p. 50.
- [Gra19] Raffaele Gratton et al. “What is a globular cluster? An observational perspective”. *The Astronomy and Astrophysics Review* **27**, 1 (2019), p. 8.
- [Ili16] C. Iliadis et al. “ON POTASSIUM AND OTHER ABUNDANCE ANOMALIES OF RED GIANTS IN NGC 2419”. *The Astrophysical Journal* **818**, 1 (2016), p. 98.
- [Kik90] S.W. Kikstra et al. “The  $^{40}\text{Ca}$  level scheme investigated with the  $^{39}\text{K}(p, \gamma)^{40}\text{Ca}$  reaction”. *Nuclear Physics A* **512**, 3 (1990), pp. 425–465.
- [Lan93] G. E. Langer, R. Hoffman, and C. Sneden. “SODIUM-OXYGEN ABUNDANCE ANTICORRELATIONS AND DEEP MIXING SCENARIOS FOR GLOBULAR CLUSTER GIANTS”. *Publications of the Astronomical Society of the Pacific* **105**, 685 (1993), p. 301.
- [Lee66] H.P. Leenhouts and P.M. Endt. “Gamma decay of levels in  $^{40}\text{Ca}$  measured with the  $^{39}\text{K}(p, \gamma)^{40}\text{Ca}$  reaction”. *Physica* **32**, 2 (1966), pp. 322–336.
- [Lon10] R. Longland et al. “Charged-particle thermonuclear reaction rates: I. Monte Carlo method and statistical distributions”. *Nuclear Physics A* **841**, 1 (2010), pp. 1–30.
- [Lon18] R. Longland, J. Dermigny, and C. Marshall. “Reaction rates for the  $^{39}\text{K}(p, \gamma)^{40}\text{Ca}$  reaction”. *Phys. Rev. C* **98** (2 2018), p. 025802.
- [Lon23] R. Longland. RatesMC. <https://github.com/rlongland/RatesMC>. 2023.

- [Mar19] Caleb Marshall et al. “The Focal-Plane Detector Package on the TUNL Split-Pole Spectrograph”. *IEEE Transactions on Instrumentation and Measurement* **68**, 2 (2019), pp. 533–546.
- [Muc12] A. Mucciarelli et al. “News from the Galactic suburbia: the chemical composition of the remote globular cluster NGC 2419”. *Monthly Notices of the Royal Astronomical Society* **426**, 4 (2012), pp. 2889–2900.
- [Muc15] Alessio Mucciarelli et al. “POTASSIUM: A NEW ACTOR ON THE GLOBULAR CLUSTER CHEMICAL EVOLUTION STAGE. THE CASE OF NGC 2808\*”. *The Astrophysical Journal* **801**, 1 (2015), p. 68.
- [Muc17] Mucciarelli, A., Merle, T., and Bellazzini, M. “The potassium abundance in the globular clusters NGC 104, NGC 6752 and NGC 6809”. *A&A* **600** (2017), A104.
- [Por56] C. E. Porter and R. G. Thomas. “Fluctuations of Nuclear Reaction Widths”. *Phys. Rev.* **104** (2 1956), pp. 483–491.
- [Pra07] Nikos Prantzos, Corinne Charbonnel, and Christian Iliadis. “Light nuclei in galactic globular clusters: constraints on the self-enrichment scenario from nucleosynthesis”. *Astronomy and Astrophysics* **470** (2007), pp. 179–190.
- [Sal13] A. L. Sallaska et al. “STARLIB: A NEXT-GENERATION REACTION-RATE LIBRARY FOR NUCLEAR ASTROPHYSICS”. *The Astrophysical Journal Supplement Series* **207**, 1 (2013), p. 18.
- [Sbo07] Sbordone, L. et al. “The exotic chemical composition of the Sagittarius dwarf spheroidal galaxy”. *A&A* **465**, 3 (2007), pp. 815–824.
- [Set67] Kamal K. Seth et al. “Study of Proton Particle-Hole States in  $^{40}\text{Ca}$  by the  $^{39}\text{K}(\text{He}^3, d)^{40}\text{Ca}$  Reaction”. *Phys. Rev.* **164** (4 1967), pp. 1450–1474.
- [Tho06] I. J. Thompson. FRESCO. <http://www.fresco.org.uk/>. 2006.
- [Tho88] Ian J. Thompson. “Coupled reaction channels calculations in nuclear physics”. *Computer Physics Reports* **7**, 4 (1988), pp. 167–212.
- [Ven12] Paolo Ventura et al. “SUPER-AGB–AGB EVOLUTION AND THE CHEMICAL INVENTORY IN NGC 2419”. *The Astrophysical Journal Letters* **761**, 2 (2012), p. L30.
- [Wan21] Meng Wang et al. “The AME 2020 atomic mass evaluation (II). Tables, graphs and references\*”. *Chinese Physics C* **45**, 3 (2021), p. 030003.
- [Wei09] H. A. Weidenmüller and G. E. Mitchell. “Random matrices and chaos in nuclear physics: Nuclear structure”. *Rev. Mod. Phys.* **81** (2 2009), pp. 539–589.

- [Yam94] T. Yamaya et al. “Cluster structure in  $^{40}\text{Ca}$  via the  $\alpha$ -transfer reaction”. *Nuclear Physics A* **573**, 1 (1994), pp. 154–172.

## **APPENDIX**

APPENDIX

A

$^{40}\text{Ca}$  ENERGY CALIBRATIONS